Local erythropoiesis directs oxygen availability in bone fracture repair

Annemarie Lang[1,2], Joseph M. Collins[1,3], Madhura P. Nijsure[1,3], Simin Belali[4,5], Mohd Parvez Khan[1], Yasaman Moharrer[1,3], Ernestina Schipani[1], Yvette Y. Yien[6], Yi Fan[7], Michael Gelinsky[2], Sergei A. Vinogradov[4,5], Cameron Koch[7], Joel D. Boerckel[1,3]

Affiliations:

[1]Department of Orthopaedic Surgery, University of Pennsylvania, Philadelphia, PA, USA

[2]Centre for Translational Bone, Joint and Soft Tissue Research, University Hospital Carl Gustav Carus, Faculty of Medicine, Technische Universität Dresden, Dresden, Germany

[3]Department of Bioengineering, University of Pennsylvania, Philadelphia, PA, USA

[4]Department of Biochemistry and Biophysics, University of Pennsylvania, Philadelphia, PA, USA

[5]Department of Chemistry, University of Pennsylvania, Philadelphia, PA, USA

[6]Division of Hematology/Oncology, Department of Medicine and Vascular Medicine Institute, University of Pittsburgh, Pittsburgh, PA, USA

[7]Department of Radiation Oncology, University of Pennsylvania, Philadelphia, PA, USA

[#]Correspondence:

Annemarie Lang – annelang@med.umich.edu

Joel D. Boerckel – boerckel@pennmedicine.upenn.edu

Summary:

Bone fracture ruptures blood vessels and disrupts the bone marrow, the site of new red blood cell production (erythropoiesis). Current dogma holds that bone fracture causes severe hypoxia at the fracture site, due to vascular rupture, and that this hypoxia must be overcome for regeneration. Here, we show that the early fracture site is not hypoxic, but instead exhibits high oxygen tension (> 55 mmHg, or 8%), similar to the red blood cell reservoir, the spleen. This elevated oxygen stems not from angiogenesis but from activated erythropoiesis in the adjacent bone marrow. Fracture-activated erythroid progenitor cells concentrate oxygen through haemoglobin formation. Blocking transferrin receptor 1 (CD71)-mediated iron uptake prevents oxygen binding by these cells, induces fracture site hypoxia, and enhances bone repair through increased angiogenesis and osteogenesis. These findings upend our current understanding of the early phase of bone fracture repair, provide a mechanism for high oxygen tension in the bone marrow after injury, and reveal an unexpected and targetable role of erythroid progenitors in fracture repair.

Main

Tissue oxygenation varies throughout the body. Atmospheric oxygen tension, or partial pressure of oxygen (pO_2), is about 155 mmHg, which corresponds to 21% fraction of oxygen in air. In the body, arterial blood features the highest oxygen fraction of 14%. The spleen is also high in oxygen, with a fraction of 8% [1]. In contrast, bone marrow has low oxygenation, 3-4% [2]. Current dogma holds that when a bone is fractured, blood vessel rupture causes a severe lack of oxygen at the fracture site. Here we show that this understanding is flawed. That is, the early fracture is not hypoxic, but rather is high in oxygen due to local activation of erythropoiesis in the adjacent bone marrow. Bone fracture, in addition to breaking the bone matrix and rupturing blood vessels, also injures the bone marrow. In adults, bone marrow is the site of erythropoiesis, the production of new red blood cells. During erythropoiesis, erythroid progenitor cells produce haemoglobin, but whether these cells regulate oxygen levels in their niche is poorly understood. During erythroid development, developing erythroid cells actively import iron via transferrin receptor 1 (Tfrc; CD71); most of this iron is used for haem synthesis, as the oxygen-carrying prosthetic group of haemoglobin. We find that bone fracture transiently activates local erythroid progenitor cells in the nearby bone marrow, concentrating oxygen at the fracture site, but transferrin receptor blockade induces hypoxia, resulting in improved bone repair.

The early fracture site is not hypoxic

Bone fracture ruptures bone marrow blood vessels, and the resulting hematoma arrests bleeding at the fracture site. Current understanding suggests that this restricted perfusion by oxygenated blood causes severe fracture site hypoxia [3-6]. This understanding is also supported by developmental reasoning, as many aspects of fracture repair recapitulate bone development, and the developing cartilaginous skeletal rudiments are hypoxic [7,8]. Further, hypoxia-inducible factor (HIF) signalling is upregulated during [9,10] and necessary for bone repair [11,12], and in vitro chondrogenesis from stem cells can be promoted by hypoxic culture [13], via HIF signalling [8,14]. However, while measurements of oxygen levels at the fracture site have been contradictory [15-19], the low oxygen paradigm has gone unchallenged due to a lack of a mechanistic basis for high oxygen tension.

To quantify oxygen at the fracture site, we used a mouse femoral fracture model with external fixation (**Fig. 1a, b**). Bone fracture does not only disrupt the vasculature, but also injures the bone marrow; we refer to the fracture gap and adjacent bone marrow as the fracture site. (**Fig. 1b, c**). After fracture, the revascularization front proceeds from proximal to distal, with most significant vascular network disruption distal to the fracture gap [20,21] (**Fig. 1c**). We reasoned that bone marrow cells distal to the fracture would be particularly and severely hypoxic after fracture. To identify hypoxic cells, we injected mice with EF5 [22-24], which labels hypoxic cells with a sigmoid relationship [22] (**Extended Data Fig. 1**). In intact bone marrow,

EF5 marked more than 50% of cells (**Fig. 1d, Extended Data Fig. 1, 2**), consistent with previously reported bone marrow oxygen tension (< 32 mmHg, or 3-4% [2]). To our surprise, the entire fracture site at 3 days post-fracture (dpf) was EF5-negative (**Fig. 1d**), indicating an absence of hypoxic cells. We next isolated cells from the fracture site for quantitative flow cytometry. Bone fracture significantly reduced the frequency of hypoxic EF5-positive cells, compared to contralateral bone marrow, at 3, 5, and 7 dpf (**Fig. 1e; Extended Data Fig. 2**). To validate this unexpected finding, we used an orthogonal method (based on phosphorescence of Oxyphor PtG4) [25-27] to directly measure tissue oxygen tension in uninjured bone marrow and the fracture site. Contralateral bone marrow featured oxygen tension of 28.8 ± 7.0 mmHg (~4%), as reported previously [2]. The fracture site measured 57.9 ± 11.5 mmHg pO_2 (~8%) at 3 dpf, comparable to oxygen levels in the spleen (**Extended Data Fig. 3a**), a red blood cell reservoir in mice [28,29]. Oxygen levels declined over time to 30 mmHg pO_2 (4%) by 14 dpf, comparable to contralateral bone marrow (**Fig. 1f**), consistent with EF5 staining (**Fig. 1d**). These data demonstrate that the early fracture site is not hypoxic, as we long assumed, but rather features high oxygen tension and only returns to normal bone marrow levels during the bone formation phase.

Elevated oxygen is not due to angiogenesis

Oxygen is transported by erythrocytes through the vasculature, so one might expect high oxygen tension to correlate with high local vascularity; however, while oxygen tension was high at 3 dpf and declined to 14 dpf, this was anticorrelated with the vascular density in the fracture site of those same samples (R = -0.98; **Fig. 1 g, h; Extended Data Fig. 3b-d**). Further, while blood vessel rupture releases oxygen-carrying erythrocytes into the fracture site, haematoma formation rapidly stops this bleeding. Despite this, fracture site oxygen tension remained elevated beyond 7 dpf. Therefore, we next tested whether physical disruption of vessel formation by ambulatory mechanical loading [4,20] would cause hypoxia. Compliant fixation indeed disrupted vascularity, but did not induce hypoxia at the fracture site (**Fig. 1i, j**). These data suggest that high oxygen levels at the fracture site are not supplied by local angiogenesis.

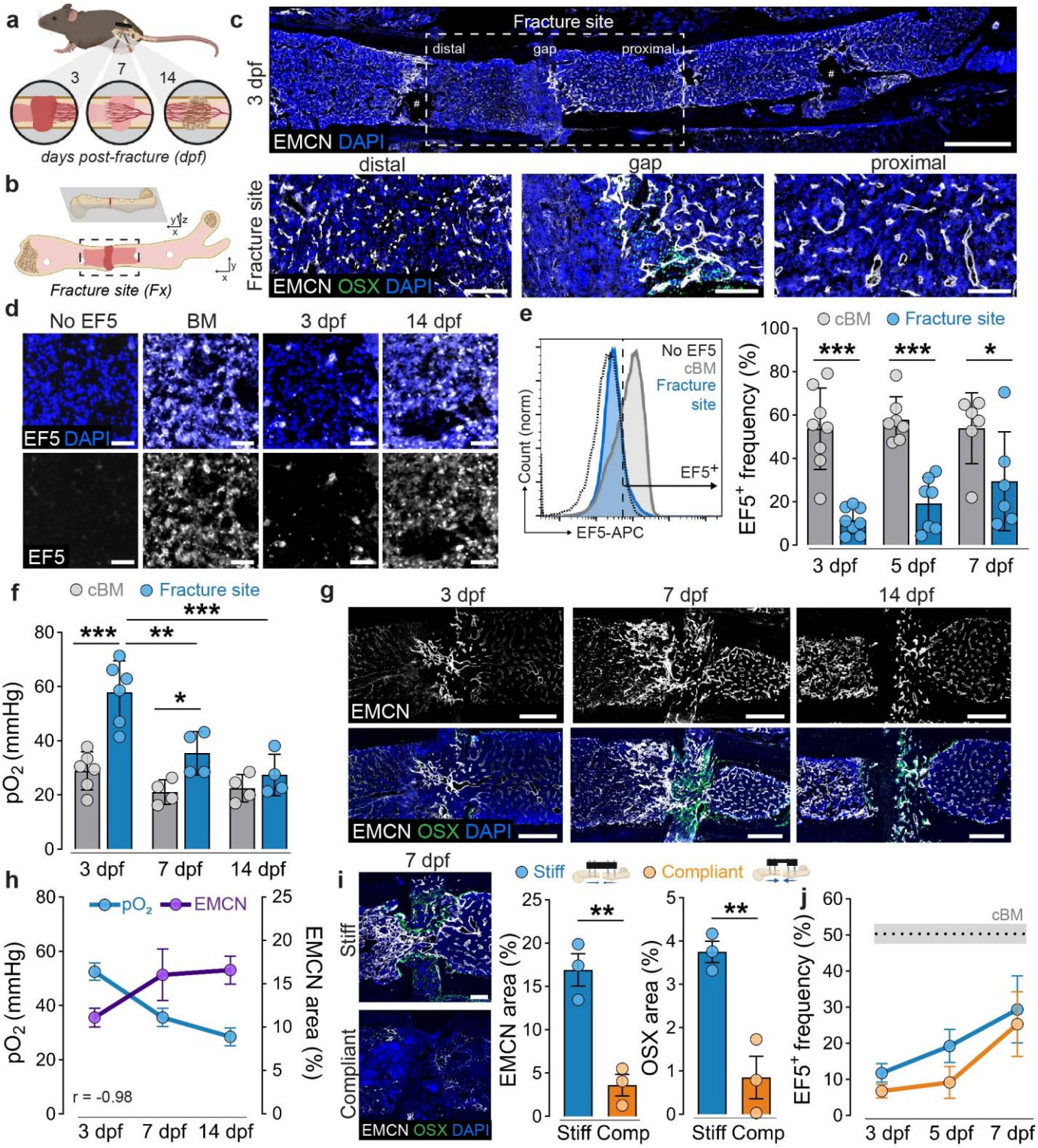

Figure 1: The early fracture site is not hypoxic. (**a**) Schematic of the fracture healing process in mice over 14 days post fracture (dpf), illustrating hematoma at 3 dpf, revascularization at 7 dpf and cartilage/bone formation at 14 dpf [30]. (**b**) We refer to the fracture site as the fracture gap and adjacent bone marrow [30]. (**c**) Immunofluorescent localization of EMCN$^+$ vessel formation and OSX$^+$ osteoprogenitor infiltration along the revascularization front at 3 dpf. Scale bars, 1 mm (top) and 200 µm (bottom). #Pin holes caused by external fixator device are exemplarily marked. (**d**) We injected mice with EF5 for immunolocalization of hypoxic cells in uninjured bone marrow (BM), and the fracture site at 3 and 14 dpf. Scale bars, 50 µm. Representative images from n = 3-4 mice per group in 3 independent experiments. (**e**) Flow cytometry analysis showing representative histograms and quantification of EF5$^+$ cell frequency in no-EF5 control, contralateral bone marrow (cBM) and fracture site cells at 3, 5 and 7 dpf. Data show individual data points for n = 6-8 mice per group and timepoint from up to 5

independent experiments and are mean ± s.d. *P* values were calculated using two-way ANOVA with Šidák multiple comparison test at each timepoint. *P* (cBM vs. Fx) < 0.001. (**f**) We used Oxyphor PtG4 to directly measure oxygen tension (pO_2) in contralateral bone marrow (cBM) the fracture gap at 3, 7, and 14 dpf. Data show individual data points for n = 4-6 mice per group and timepoint from at least 2 independent experiments and are mean ± s.d. *P* values were calculated using two-way ANOVA with Tukey multiple comparison test for preselected comparisons. *P* (cBM vs. Fx; time; interaction) < 0.01. (**g**) Immunofluorescent localization of EMCN and OSX, indicating revascularization from proximal to distal. Scale bars, 200 µm. Representative images from n = 3-6 mice per timepoint in 3 independent experiments. (**h**) Quantification and correlation analysis of pO_2 (mean of fracture site) and $EMCN^+$ area (total fracture site) in the same samples. Data are mean ± s.e.m. for n = 4-6 mice per group and timepoint from at least 2 independent experiments. Pearson correlation coefficient: R = -0.98, *P* = 0.12. (**i**) Immunofluorescent localization of EMCN and OSX at 7 dpf under stiff and compliant fixation [30]. Scale bars, 400 µm. Data show individual data points for n = 3 mice per group and are mean ± s.e.m. *P* values were calculated using two-tailed Student's *t*-test. **P* < 0.05, ***P* < 0.01 and ****P* < 0.001. (**j**) Quantification of $EF5^+$ cell frequency under stiff and compliant fixation. Data are mean ± s.e.m for n = 4-7 mice per group per timepoint from 5 independent experiments.

Bone marrow contains oxygen-binding erythroid cells

Bone marrow contains resident hematopoietic stem and progenitor cells (HSPCs) that create new red blood cells through erythropoiesis. We used single cell RNA-sequencing to identify cell populations in contralateral bone marrow and the fracture site at 3 dpf (**Fig. 2a**). We identified eight major cell clusters by canonical marker expression (**Fig. 2b, c; Extended Data Fig. 4**). Innate immune cells, including monocytes, macrophages and granulocytes, represented the majority of cells at the fracture site, consistent with known inflammation kinetics [21,31,32] (**Extended Data Fig. 4**). Other cell types included HSPCs, adaptive immune cells (T- and B-cells) and erythroid progenitors (**Extended Data Fig. 5**). Relative to contralateral bone marrow, bone fracture upregulated genes involved in oxidative phosphorylation across all cell types, particularly in HSPCs, neutrophils, and erythroid progenitors (**Extended Data Fig. 6**). Erythroid-lineage cells bind oxygen by iron-containing haemoglobin (**Fig. 2d**) and are characterized by expression of the transcription factor *Gata1*, the membrane protein *Glyphorin A (Gypa)*, and the iron importer *Transferrin receptor (Tfrc)* [33-35] (**Fig. 2c**). Haemoglobin synthesis in erythroid progenitors includes production of haem. Haem is synthesized through multiple enzymatic steps in the cytosol and mitochondria, culminating in the insertion of Fe^{2+} ion into the porphyrin ring[36] (**Fig. 2d**). Simultaneously, globin proteins are produced in the cytoplasm (**Fig. 2d**). We found bone marrow erythroid progenitor cells at the fracture site, marked by expression of genes responsible for the haem synthesis and adult globin (**Fig. 2e,f**). Gene set enrichment analysis suggests that bone fracture induced erythroid progenitor proliferation at the fracture site (**Fig. 2g**). Thus, fracture of a bone that contains bone marrow may amplify erythroid progenitor cells at the fracture site, which could influence local oxygen concentration.

The normal bone marrow niche measures 4% oxygen fraction and contains both EF5-positive and EF5-negative cells (**Fig. 2h**). In contrast, the highly-oxygenated spleen exhibits minimal EF5 positivity (**Fig. 2h**). We gated $CD71^+$ $Ter119^+$ bone marrow erythroid cells from non-erythroid cells and quantified intracellular oxygenation by EF5 staining (**Fig. 2i, j**). Most

non-erythroid cells were EF5-positive (i.e., low oxygen), while most erythroid cells were EF5-negative (i.e., high oxygen) (**Fig. 2i, j; Extended Data Fig. 7**). Whether erythroid progenitor cells in uninjured bone marrow bind oxygen is unclear. Here we demonstrate that fracture-activated erythroid progenitor cells induce haemoglobin and bind oxygen. This is consistent with oxygen binding by haemoglobin in other non-erythrocyte cells such as chondrocytes [37], neurons [38], muscles [39], and immune cells [40].

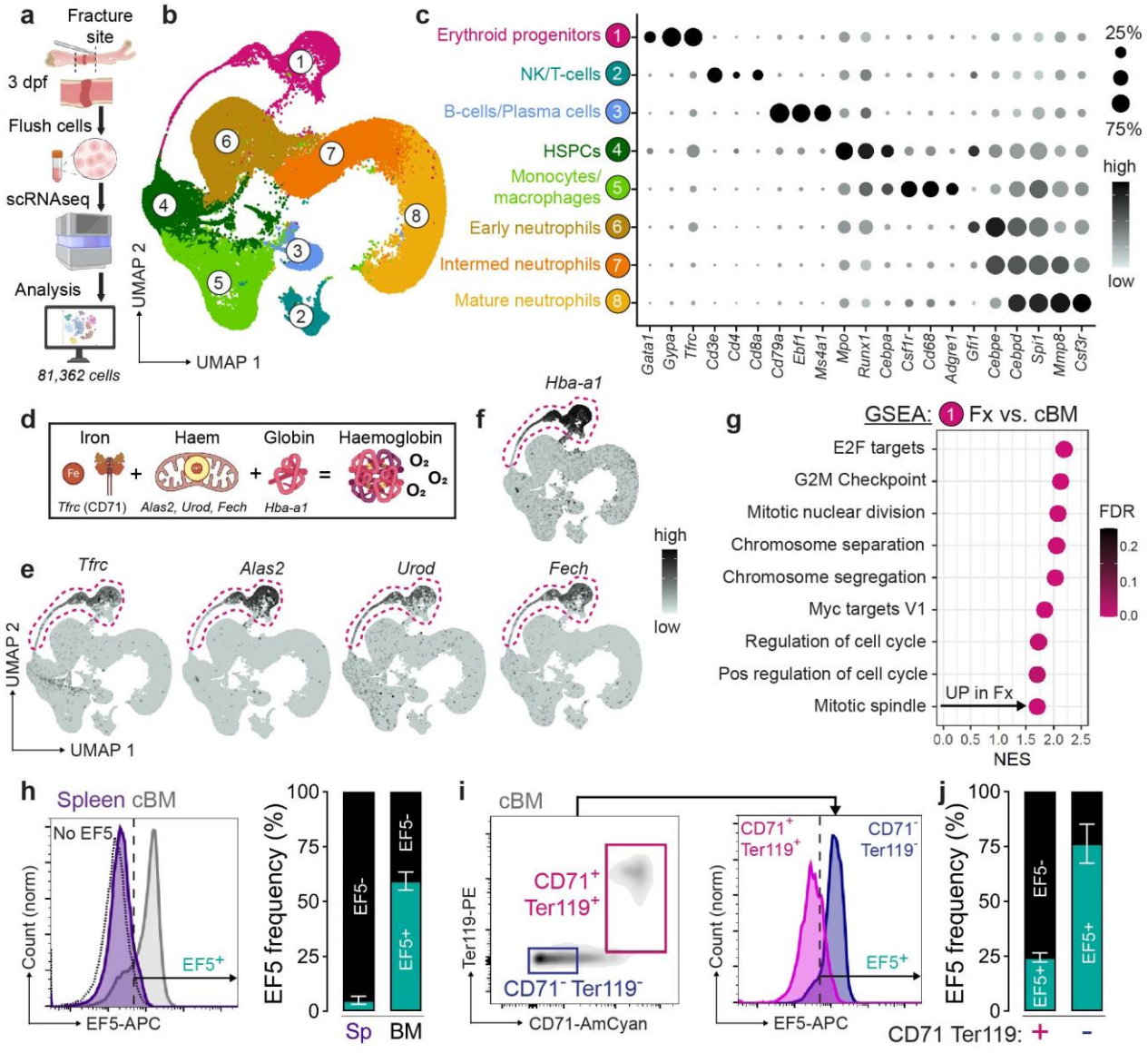

Figure 2: Erythroid progenitors express molecular machinery for oxygen binding. (**a**) Schematic illustrating scRNA-sequencing of cells flushed from the fracture site at 3 dpf (Fx) or the contralateral bone marrow (cBM). We removed dead cells and lysed mature red blood cells, but did not digest the samples or sort prior to scRNA-seq [30]. (**b**) UMAP and Louvain clustering. Integrated data sets from n = 3 mice per group from 3 independent experiments. (**c**) Cell type annotations based on canonical marker expression. (**d**) Schematic illustration of haemoglobin synthesis [30] and (**e, f**) feature plots of relevant genes on the UMAP. (**g**) Gene set enrichment analysis (GSEA) highlighting upregulated pathways and processes in erythroid progenitors at the fracture site compared to cBM. (**h**) Representative histogram and quantification of EF5 staining in bone marrow (BM) and spleen (Sp). Data are mean ± s.e.m. for n = 5-10 mice from at least 5 independent experiments.

(**i, j**) Flow cytometry analysis of erythroid lineage cells ($CD71^+$ $Ter119^+$) compared to non-erythroid ($CD71^-$ $Ter119^-$) cells. Data are mean ± s.e.m. for n = 4 mice from 4 independent experiments.

Fracture induces local erythropoiesis

To test whether fracture activates bone marrow erythroid cells, we performed secondary Louvain clustering on the erythroid progenitor cell cluster. We identified seven erythroid progenitor cell states, which we assigned to three different developmental stages based on lineage-specific gene expression profiles [41]: megakaryocytic-erythroid progenitors (MEP), proerythroblasts (ProE), and erythroblasts (EryB) (**Fig. 3a, b**). Cells from the fracture site contained a significantly higher frequency of ProE cells compared to contralateral bone marrow, as measured by both scRNA-seq (**Fig. 3c**) and flow cytometry [42] (**Fig. 3d,e; Extended Data Fig. 8a**). Further, bone fracture reduced the frequency of EryB cells while increasing the number of peripheral blood reticulocytes at 3 dpf, suggesting accelerated maturation (**Fig. 3f; Extended Data Fig. 8a**). However, the serum concentration of the erythropoietic hormone, erythropoietin (Epo), was not elevated at 3 dpf (**Fig. 3g**), indicative of local, but not systemic, erythropoietic activation. To spatially visualize this local erythropoiesis, we immunostained for CD71 and Ter119-expressing erythroid cells. Fracture increased erythroid cell abundance adjacent to the fracture site, but the contralateral (i.e., opposite limb) and ipsilateral bone marrow (i.e., same limb but far from the fracture site) exhibited similar, homeostatic levels of $CD71^+$ $Ter119^+$ erythroid cells (**Fig. 3h**). Fracture site-adjacent $CD71^+$ erythroid cells declined in abundance from 3 to 14 dpf (**Fig. 3j; Extended Data Fig. 8b-d**), paralleling the decrease in O_2 levels (cf. **Fig. 1h**). These findings indicate that fracture induces local, but not systemic, erythropoiesis in the bone marrow adjacent to the fracture site.

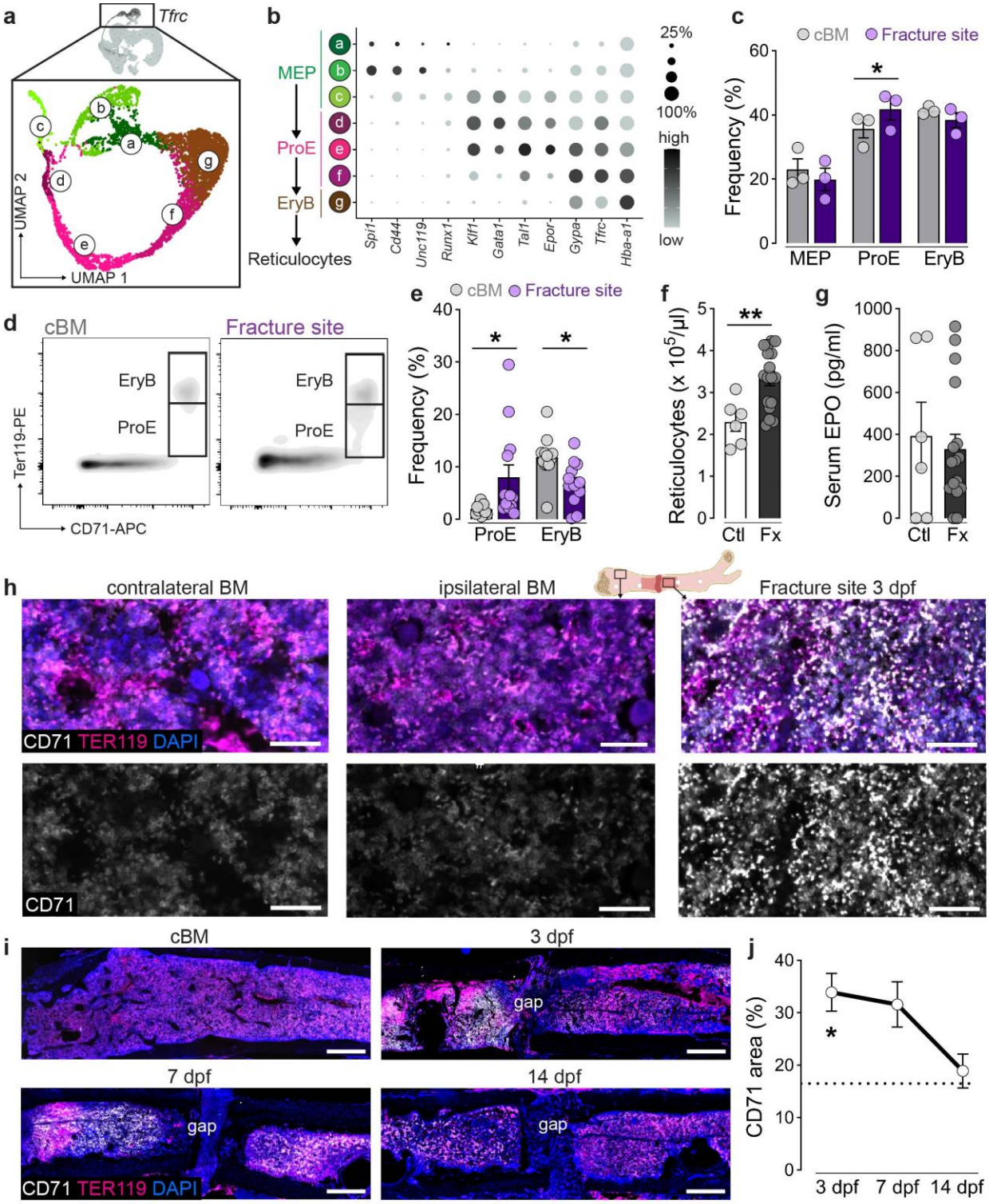

Figure 3: Bone fracture activates local erythropoiesis at the fracture site. (**a**) Secondary Louvain clustering of erythroid progenitor cells. Integrated data sets from n = 3 mice per group from 3 independent experiments. (**b**) Erythroid cell differentiation state annotations based on developmental stage-specific marker expression. (**c**) Frequency of cells in the different clusters normalized to the absolute cell count per cluster. Data show individual data points from n = 3 mice per group from 3 independent experiments and are mean ± s.e.m. *P* values were calculated using two-tailed paired Student's *t*-test. (**d**) Flow cytometry analysis and representative histograms of ProE and EryB based on Ter119 marker intensity. (**e**) Frequencies of ProE (Ter119^{med} CD71^{high}) and EryB (Ter119^{high} CD71^{high}). Data show individual data points from n = 13 mice from more than 5 independent experiments and are mean ± s.e.m. *P* values were calculated using one-way ANOVA with Šidák multiple comparison test for preselected pairs. (**f**) Concentration of reticulocytes in peripheral blood. Data show

individual data points from n = 6-17 mice from more than 5 independent experiments and are mean ± s.e.m. *P* values were calculated using two-tailed Student's *t*-test. (**g**) Serum concentration of Erythropoietin (EPO) in peripheral blood. Concentration of reticulocytes in peripheral blood. Data show individual data points from n = 6-17 mice from more than 5 independent experiments and are mean ± s.e.m. *P* values were calculated using two-tailed Student's *t*-test. (**h**) Immunolocalization of Ter119 and CD71 positive cells in contralateral and ipsilateral bone marrow and at the fracture site [30]. We refer to the ipsilateral bone marrow as the bone marrow regions in the injured bone but distant from the fracture site. Scale bars, 50 µm. Representative images for n = 4-8 mice per timepoint from 3 independent experiments. (**i**) Representative images of Ter119 and CD71 positive cells in the cBM and at the fracture site at 3, 7 and 14 dpf. Scale bars, 500 µm. (**j**) Quantification of CD71 positive area as sum of distal and proximal fracture site over time. Dashed line indicates normal bone marrow control. Data are mean ± s.e.m. for n = 4-8 mice per timepoint from 3 independent experiments. *P* values were calculated using one-way ANOVA with Tukey multiple comparison test. $*P < 0.05$, and $**P < 0.01$.

Erythroid progenitors concentrate oxygen at the fracture site

Next, we sought to determine how local erythropoiesis increased oxygen at the fracture site and the impact on fracture repair. During their maturation, erythroid progenitor cells import large quantities of iron to support haemoglobin formation and oxygen binding [43,44]. The primary iron importer in erythroid cells is Transferrin receptor 1 (CD71, encoded by *Trfc*) (**Fig. 2c, e**). Therefore, to block iron import in cells at the fracture site, we locally injected a CD71-blocking antibody (or isotype control IgG) immediately after fracture (**Fig. 4a**). CD71 blockade had no effect on the increase in erythroid cell numbers at the fracture site (**Fig. 4b; Extended Data Fig. 9a**), but, in erythroid cells, significantly downregulated the expression of genes required for haem synthesis (**Fig. 4c; Extended Data Fig. 9b**). Further, CD71 blockade significantly reduced oxygen at the fracture site, measured by EF5 and independently by Oxyphor PtG4 (**Fig. 4d, e; Extended Data Fig. 9c**), returning oxygen tension in the fracture site at 3 dpf to the level of native bone marrow (~5%; **Fig. 4f**). Importantly, in erythroid cells at the fracture site, CD71 blockade significantly increased EF5-positivity, establishing that CD71 blockade decreased oxygenation of the erythroid progenitors per se (**Fig. 4f; Extended Data Fig. 9d**). Further, CD71 blockade significantly enhanced bone formation (**Fig. 4h, i; Extended Data Fig. 10**), osteoprogenitor activation, and angiogenesis at the fracture site at 14 dpf (**Fig. 4j, k**). Together, these findings suggest that bone fracture-activated erythroid progenitors concentrate oxygen at the fracture site, but preventing erythroid cell haemoglobin production creates fracture site hypoxia and enhances repair.

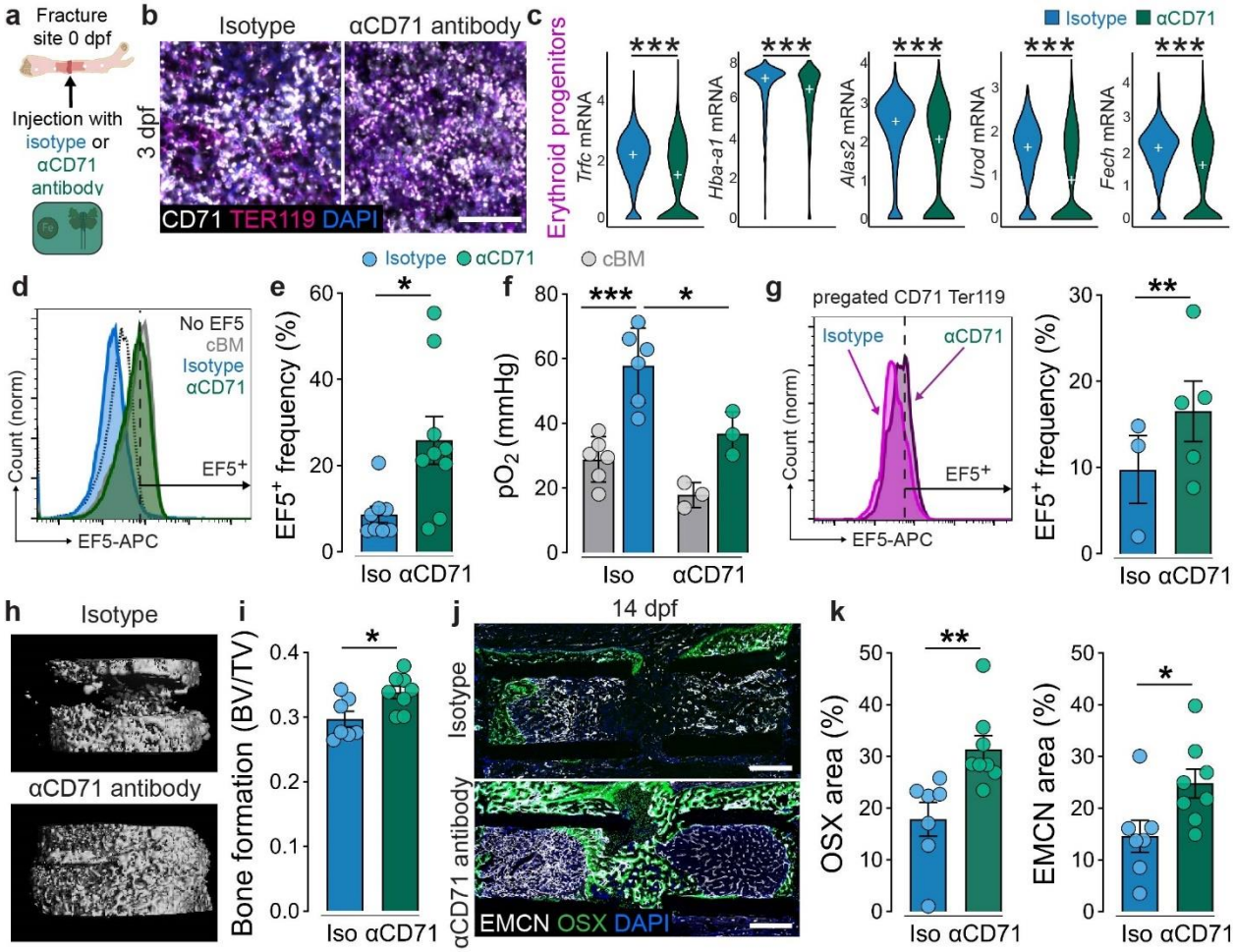

Figure 4: CD71 blockade induces hypoxia and promotes fracture repair. (**a**) CD71 blocking antibody, or isotype control IgG, were injected into the fracture gap immediately after fracture [30]. (**b**) Immunolocalization of Ter119 and CD71 positive cells at the fracture site at 3 dpf after αCD71 antibody treatment. Scale bar, 50 µm. Representative image for n = 3 mice from 3 independent experiments. (**c**) Erythroid cell expression of genes involved in haem synthesis. Integrated data sets from n = 3 mice per group from 3 independent experiments. White cross indicates median. *P* values were calculated using MAST with Bonferroni corrections. P_{adj}: *Trfc* = 2.3E-46; *Hba-a1* = 9.8E-29; *Alas2* = 3.0E-41; *Urod* = 8.0E-46; *Fech* = 1.0E-40. (**d**) Flow cytometry analysis of EF5 frequency displaying representative histogram and (**e**) quantification of $EF5^+$ cell frequency in cells isolated from the fracture site at 3 dpf. Data show individual data points for n = 8-9 mice per group from 5 independent experiments and are mean ± s.e.m. *P* values were calculated using two-tailed Student's *t*-test. (**f**) Direct measurement of oxygen tension in the fracture gap and cBM at 3 dpf. Data for Iso are reproduced from Fig. 1f. αCD71 data show individual data points for n = 3 mice from 3 independent experiments and are mean ± s.d. *P* values were calculated using one-way ANOVA with Šidák multiple comparison test for preselected comparisons. (**g**) Flow cytometry analysis of EF5 positivity in erythroid lineage cells ($CD71^+$ $Ter119^+$) at 3 dpf. Data show individual data points for n = 3-5 mice per group from 3 independent experiments and are mean ± s.e.m. *P* values were calculated using two-tailed paired Student's *t*-test. (**h, i**) MicroCT analysis of bone formation (bone volume/total volume) at 14 dpf. (**j, k**) Immunofluorescence analysis of $EMCN^+$ vessel formation and OSX^+ progenitor infiltration at the fracture site at 14 dpf. Scale bars, 500 µm. Data show individual data points for n = 9-10 mice per group from 2 independent experiments and are mean ± s.e.m. *P* values were calculated using two-tailed Student's *t*-test. **P* < 0.05, ***P* < 0.01 and ****P* < 0.001.

Conclusions

Here we demonstrate that the early fracture site is not hypoxic, as long believed, but rather that bone fracture acutely activates local erythroid progenitor cells, concentrating oxygen at the fracture site. Blockade of the iron transporter necessary for oxygen binding by haemoglobin induces hypoxia, resulting in improved bone repair. These findings provide a mechanistic basis for high oxygen tension in the fracture gap, and reveal a previously unrecognized and targetable role of erythroid progenitors in fracture repair.

Our findings upend the widely held understanding that the fracture site is severely hypoxic and that this hypoxia must be overcome to enable regeneration. We show using multiple orthogonal methods that the early fracture site is not hypoxic and that high oxygen levels at the fracture site impair regeneration. Oxygen tension at the fracture site was first reported by Brighton and Krebs in 1972 [16]. Using the rabbit fibula as a model, they measured the fracture haematoma to be hypoxic (6.3 mmHg). However, the rabbit fibula contains minimal bone marrow and no significant erythropoietic activity [45]. Our data are consistent with data from a sheep tibial osteotomy model [17], which like most long-bone injuries involves the bone marrow. Although the fracture site begins with high oxygen, we show that inducing hypoxia by iron transporter blockade promotes regeneration, consistent with the importance of hypoxia inducible factor (HIF) signalling in fracture repair [9,12] and with studies investigating HIF signalling gain-of-function as a therapeutic approach [46,47].

Mature red blood cells carry oxygen throughout the body, but whether immature erythroid progenitor cells are also capable of binding oxygen and whether this matters is poorly understood. Here, we show that bone marrow-resident erythroid progenitor cells can influence their local oxygen environment and that this is functionally relevant in the context of fracture repair. We do not yet know the molecular mechanisms by which bone fracture activates local erythropoiesis. Fracture activation of erythropoiesis occurs locally, without systemic change in EPO, but coincides with macrophage mobilization to the fracture site. In the bone marrow, erythropoiesis is regulated under homeostasis and stress by specialized macrophages in erythroblastic islands [48,49]. Therefore, we speculate that localized erythropoiesis in the bone marrow could be dependent on local macrophage activation [32,50].

Blood vessels and angiogenesis are critical to fracture healing. Disruption of blood vessel formation, whether genetic, pharmacologic, or mechanical alters the course of repair, particularly stimulating cartilaginous callus formation [20,51-54]. We and others previously attributed this chondrogenesis to reduced oxygen transport [20,51]. However, here we found that while compliant fixation induced cartilage callus formation [55], mechanical disruption of angiogenesis did not induce fracture site hypoxia. This suggests that elevated local pO_2 is not due to local angiogenesis. This is consistent with a recent study demonstrating that disruption of neovascular ingrowth during bone repair induces chondrogenesis because of limited

nutrient supply, particularly of fatty acids, rather than limited oxygen [56]. Further, our observation that fracture upregulated genes involved in oxidative phosphorylation in cells of the fracture gap, suggests an increase in the respiratory activity and makes it more likely that the elevated pO_2 in the fracture is caused not by a decrease in cellular oxygen consumption but by oxygen concentration by erythroid cells.

We speculate that haemoglobin-producing erythroid progenitor cells function as a local oxygen sink, creating an oxygen gradient as oxygen diffuses from surrounding vascularized tissues toward the fracture site. This transiently maintains high oxygen tension at the fracture site as long as oxygen diffusion outpaces consumption, but blockade of erythroid iron transport prevents formation of the oxygen sink and resultant oxygen gradient. Consistently, we observed an inverse relationship between fracture site oxygenation and local vascular density, characterized by decreasing oxygen with blood vessel invasion. We speculate that the recovery of bone marrow hypoxia promotes angiogenesis, allowing for maturation and extravasation of the erythroid cells, clearing the fracture site.

These findings may also change how we think about the evolution of fracture repair. Producing a high oxygen environment that delays repair seems evolutionarily counterproductive. We speculate a trade-off between making a maximally hospitable environment for healing vs. fighting microbial infection [57,58], during the window of greatest infection risk after fracture. Thus, high oxygen at the fracture site may prioritize pathogen control at the expense of delayed regeneration. Together, our work identifies an unexpected role of erythroid progenitors in regulating oxygenation of the bone marrow niche, which may be targetable to promote regeneration.

Methods

Mouse femoral fracture model

Female or male C57BL/6J mice were obtained from The Jackson Laboratory at age 10 weeks and used within 2-6 weeks. All procedures adhered to IACUC regulations (University of Pennsylvania; protocol no: 806482). Veterinary care and husbandry were provided by University Laboratory Animal Resources (ULAR) at the University of Pennsylvania, following contemporary best practices. Mice were housed in a semi-barrier facility with a 12/12-hour light/dark cycle (light from 7:00 a.m. to 7:00 p.m.), a room temperature of 72 ± 2°F, and a humidity of 50 ± 10%. Food and tap water were available *ad libitum*. Mice were randomly paired per cage, which contained wooden chips, Enviro-dri, and shredded paper towels as bedding and nesting material. Additional enrichment included a clear mouse transfer tube (Braintree Scientific), a mouse double swing (Datesand Group), and a Shepherd Shack (Shepherd Specialty Papers) with an enlarged entrance to prevent injuries [59]. The transfer tube and double swing were removed post-surgery to reduce injury risk. Mice were handled with the transfer tube, and cages were changed weekly.

Mouse femoral fracture model: Mice were induced with isoflurane (2–3% in 100% oxygen) and placed on a 37 °C heating pad. Anaesthesia was maintained at 1.5–2% with a nose cone. Eye ointment, physiological saline (0.9% sodium chloride; 0.5 ml, s.c.) and clindamycin (45 mg/kg, s.c.) were administered. Buprenorphine SR-Lab (1 mg/kg, s.c.; Wedgewood Pharmacy) or Ethiqa XR (extended release buprenorphine; 3.25 mg/kg, s.c.; Fidelis Animal Health) were used for analgesia. The left femur was shaved and disinfected with iodine solution and 70% ethanol. A longitudinal incision was made between the knee and hip, and the musculus vastus lateralis and musculus biceps femoris were separated to expose the femur. Two external fixators (stiff: 18.1 N/mm; compliant: 3.2 N/mm [60], RISystem) were used to modulate ambulatory load transfer. The fixator bar was aligned parallel to the femur, and pins were inserted after pre-drilling. A 0.5 mm fracture gap was created using a Gigli wire saw (0.44 mm; RISystem) and flushed with saline. Muscle and skin were sutured in two layers, and the wound was treated with antibiotic cream. Mice were returned to their home cages, placed under an infrared lamp, and monitored until fully recovered. Diet Gel was provided on the cage floor to ensure post-surgery food and water intake. Mice were closely monitored and scored for the first 4 days, then on days 7 and 10, before euthanasia. Scoring included a composite score based on the mouse grimace score (eyes and ears only), clinical score, and a model-specific score for limping and dragging, following established systems [61,62]. Humane endpoints were predefined, including criteria such as wound dehiscence, poor grooming, sunken eyes, hunched posture, periprosthetic fracture, severe axial deviation, lack of food and water intake, significant weight loss, bloody faeces, severe respiratory issues, debilitating diarrhoea, seizures, paresis, and abscesses. No humane endpoints were reached during the study. Mice were euthanized at different timepoints post-surgery using CO_2 and cervical dislocation. Samples were collected as described below. All analyses were performed blind to the groups (fixation, treatment), with de-blinding only after all analyses were completed to avoid bias.

EF5 cell staining

To identify hypoxic cells, we used EF5, which, as an inverse function of oxygen, is reduced by nitroreductase enzymes to form cytoplasmic EF5-protein adducts that can be identified by immunostaining [22-24].

In vivo experiments: Mice were injected with the hypoxia marker EF5 (10 µl/gm of 10 mM solution) and euthanized using CO_2 and cervical dislocation after 2h. As a negative control for in situ EF5 labelling of cells with known high pO_2, we performed EF5 staining of the spleen (nominal pO_2 of 8-10%). As a positive control for *in sit*u EF5 labelling of marrow cells in low oxygen conditions, mice were similarly injected with 10 mM EF5 but euthanized after 30 min. The body was then kept at 37°C for 45 min (termed euthanized animal control, EAC) to allow all EF5 to be biochemically reduced in place. To control for any nonspecific background staining, we also included bone marrow cells from non-EF5 treated animals ($EF5^-$). For subsequent EF5 staining on frozen sections, fractured femora were cryo-embedded (Tissue-Tek OCT) without previous fixative treatment and stored at -80 °C until further use. For flow cytometry, cells were flushed from the fracture site (i.e.,

region between the inner pins), the adjacent bone marrow of the same limb and the bone marrow from the uninjured contralateral bone. Flushed cells were immediately fixed with 4% paraformaldehyde for 1h on ice.

EF5 staining on cryosections: Consecutive 7 µm-thick sections were prepared using cryotape (Sectionlab). Sections were fixed onto glass slides and stored at -80 °C until staining. Before staining, sections were fixed in 4% paraformaldehyde, blocked with 5% goat serum, and stained 4h with Anti-EF5 antibody, clone ELK3-51 Cyanine 3 conjugate dissolved in PBS/3% BSA/0.1% Tween 20 (stock: 2 mg/mL; 1:25 to get 80 µg/ml). Sections from positive and negative controls were used to adjust imaging settings.

In vitro experiments: Bone marrow cells were flushed from femora of C57BL/6J female mice and transferred into culture medium (MEM + 5% FCS supplemented with HEPES and bicarbonate as buffer system and 100 µM EF5 compound). Cells were cultured without CO_2 in aluminium chambers (shaken at ~ 1Hz) for 2h at 37°. The gas phase in the chambers contained 10%, 2%, 0.5%, 0.1% fraction of oxygen (pO_2). Cells were rinsed, then fixed with 4% paraformaldehyde for 1h on ice.

EF5 staining and flow cytometry: Fixed cells were washed with PBS and stained over night with Anti-EF5 Antibody, clone ELK3-51 Antibody, Cyanine 5 conjugate (stock: 2 mg/mL; 1:200 to get 10 µg/ml) dissolved in PBS/1.5% BSA/1.5% non-fat dry milk/0.3% Tween 20/5% mouse serum at 4°C under constant shaking. Cells were carefully washed twice with PBS/0.3% Tween 20 and once with PBS (30 min each). In case of additional staining, antibodies were diluted in PBS/2% FCS/0.3% Tween 20 and incubated on the cells for 30 min before additional washing steps and secondary fixation (PBS/1% PFA). The following antibodies were used: CD71-APC (BioLegend; clone: RI7217; catalogue number: 113819; 1:100); Ter119-PE (BioLegend; catalogue number: 116207; 1:100); CD71- Brilliant Violet 510 (AmCyan; BioLegend; catalogue number: 113823; 1:100); CD45-Brilliant Violet 510 (AmCyan; BioLegend; catalogue number: 103137; 1:200). Non-EF5 treated and no-antibody controls were conducted for every experiment. Cells were analysed using a FACSCanto II flow cytometer (BD Biosciences) and the FlowJo software (V10).

Immunofluorescent staining

Femora were fixed for 6h in 4% paraformaldehyde at room temperature and were then transferred into 10% ethylenediaminetetraacetic acid (EDTA) pH 7.4 for 3 days at 4 °C followed by treatment with 30% sucrose solution for 2 days before being cryo-embedded using Tissue-Tek OCT. Consecutive sections of 7 µm were prepared using cryotape (Sectionlab). Sections were fixed onto glass slides and stored at -20 °C until staining. Cryosections were rehydrated in PBS. Blocking solution (10% goat serum/PBS) was added for 30 min and antibodies were diluted in PBS/0.1% Tween20/5% goat serum. The following primary antibodies and secondary antibodies were used (incubation 2h at room temperature): EMCN (Santa Cruz; clone V.5C7; catalogue number: sc-65495; 1:100), OSX (Abcam; catalogue number: ab209484; 1:100), CD71-

APC (BioLegend; clone: RI7217; catalogue number: 113819; 1:100); Ter119-PE (BioLegend; catalogue number: 116207; 1:100); all secondary antibodies were purchased from Thermo Fisher Scientific and used at an 1:500 dilution for 2h at room temperature: goat anti-rat A488 (A-11006) and goat anti-rabbit A647 (A-27040). DAPI (1 µg/mL) was added during the last washing step and sections were covered with Fluoromount-GT. Images were taken with an AxioScan and image quantification was performed using the Fiji/ImageJ software. The area of interest was manually assigned with the built-in ROI-Manager and determined with the thresholding tool.

In vivo oxygen measurement

Oxygen measurements *in vivo* were performed by the phosphorescence quenching method [25] and the probe Oxyphor PtG4 [26,27]. Overall, our measurements closely resembled phosphorescence quenching oximetry experiments performed previously in a variety of tissue types, including recent measurements in the brain [63], intestine [64] and tumours [65]. Oxyphor PtG4 (50 µl, 50 µM; if necessary, dilution was done with saline) was injected in the tail vein 1 day prior to surgery to allow the probe to distribute evenly through tissues, ensuring that it would be present in the fracture hematoma and gap after osteotomy. Osteotomy surgery was performed as described above. At 3, 7 and 14 dpf, mice were anesthetized with isoflurane (2–3% in 100% oxygen) and placed on a heating pad (37°C). As anaesthesia may influence tissue oxygen levels, it was maintained at the level of 2% isoflurane in 100% oxygen (flow rate 1.5 L/min), delivered using a nose cone. For analgesia, Buprenex was injected s.c. (0.1 mg/kg), and an eye ointment was applied. The fractured and contralateral bones were carefully dissected and exposed. The measurement times at the fractured and contralateral bones were kept similar. Oxygen levels were measured at different locations of the bone using a fiber-optic phosphorometer (Oxyled, Oxygen Enterprises). In brief, excitation was performed using a laser diode (630 nm), focused into a spot ~200 µm in diameter on the bone surface. 630 nm light is able to diffuse into tissue reaching several mm's (up to 1cm) depths. Thus, our measurements probed average pO_2 throughout the bone under the excitation spot with dominant contributions from the regions closest to the surface. The phosphorescence was collected using a single mode plastic fiber (4 mm in diameter), which carried the light to an avalanche photodiode (Hamamatsu 12703). Excitation pulses were 10 µs-long, and the phosphorescence decays were collected and digitized (500 kHz frequency) during 500 µs after each pulse. 100 excitation/collection cycles were averaged to achieve high signal-to-noise ratios. Thus obtained phosphorescence decays were fitted to single-exponentials, and the corresponding decay times (lifetimes) were converted to pO_2 values using a calibration obtained in independent experiments, as described previously [27]. Animals were immediately euthanized after the measurements by cervical dislocation under deep anaesthesia.

Blood analysis and Epo ELISA

Blood was intracardially collected in deep anaesthesia (CO_2) before cervical dislocation. Samples for haematology were collected in EDTA tubes and transferred to the Clinical Pathology Laboratory, PennVet for complete blood count (CBC) analysis using an IDEXX ProCyte Dx Hematology Analyzer. Serum was collected in tubes with coagulation activator gel and stored at -20 °C. For assessing the serum Epo concentration, we used a Mouse Erythropoietin/EPO DuoSet ELISA kit (R&D Systems) following the manufacturer's instructions.

Antibody experiment and microCT

We injected either a monoclonal rat anti-mouse CD71 antibody (clone: 8D3; 100 µg) or a rat IgG2a isotype control (both Bio X Cell) in the fracture gap after skin closure. EF5 staining and Oxyphor measurement were performed at 3 dpf (days post fracture) as described above. MicroCT and immunofluorescence analyses were performed at 14 dpf. Ex vivo microCT scanning was conducted using a µCT 45 desktop scanner (Scanco Medical AG) following the removal of the external fixator. Bones were secured in plastic pipettes to preserve the integrity of the callus tissue. Scanning focused on the region between the inner two pins with an isotropic voxel size of 10.4 µm (55 kVp, 72 µA, AL 0.5 mm, 1x400 ms), aligning the scan axis along the femoral diaphysis. 3D reconstruction and subsequent analyses were carried out with the accompanying software package, utilizing a global threshold of 240 mg HA/cm^3. An individual VOI was determined for each sample, confined to the area between the middle pins. The analysis excluded the original cortical bone, focusing solely on newly formed bone.

Single-cell RNA sequencing

Cell isolation and preparation: Femoral fracture surgeries were performed as described above. Cells were isolated from the following samples: intact contralateral femora and fractured femora at 3 dpf, with or without CD71 antibody treatment (n = 3 mice per group). Cells were flushed from the fracture site (between middle pins) or the intact bone marrow (contralateral femur) in cold PBS and transferred through a cell strainer. Red blood cells were lysed with a Red Blood Cell Lysis kit and dead cells were then removed with a Dead Cell Removal kit (both Miltenyi Biotec) following the manufacturer's instructions. Samples were confirmed to have > 95% viability (based on trypan blue staining). Cells were resuspended in PBS/0.4% BSA and transferred on ice to the sequencing core facility.

Single-cell RNA sequencing and analysis. Next-generation sequencing libraries were created utilizing the 10x Genomics Chromium Single-cell 3' Reagent kit v3 following the manufacturer's protocols. Each library was uniquely indexed with the Chromium dual Index Kit, pooled, and sequenced on an Illumina NovaSeq 6000 in a paired-end, dual indexing run, aiming for ~ 21,092 reads per cell. Data processing involved the Cell Ranger pipeline (10x Genomics, v.6.1.2) for demultiplexing, aligning reads to the mm10 transcriptome, and generating feature-barcode matrices. Subsequent analysis employed Seurat

v4.0 [66]. Cells were ignored if they had fewer than 200 genes, more than 6000 genes, or over 5% mitochondrial reads. The data from individual samples underwent LogNormalization, and 2000 variable features were identified for each sample. Seurat's alignment method was used for sample integration, followed by data scaling with ScaleData. Principal component analysis (PCA) was performed for linear dimensional reduction. The entire 81,362-cell dataset was visualized in two dimensions using UMAP, and clustering was performed with Louvain clustering. Dimensions were 1:7 and a resolution of 0.1 was applied in the clustering analysis. The FindAllMarkers function and canonical marker genes helped identify major cell types. Louvain clustering resulted in 8 clusters, which were assigned to the respective cell populations. For gene set enrichment analysis (GSEA), a pre-ranked list of genes was generated based on fold changes between comparisons and analysed using GSEA v4.3.3. The murine hallmark gene set collection and the GO Biological Process ontology from the Molecular Signatures Database (MSigDB) was used for comparisons. Significant inter-cluster gene expression differences were identified using MAST with Bonferroni corrections. Erythroid progenitors constituted 1 of the initial 8 clusters. These cells were then sub-divided and reanalysed using the pipeline described above. Iterative clustering of the erythroid progenitors revealed 7 clusters, which were assigned to 3 cell states based on canonical marker expression and relevant literature [41].

Statistical Analysis

Power analysis was performed *a priori* for key outcome measures. Statistical analysis was conducted using GraphPad Prism version 9. To assess the Gaussian distribution, the D'Agostino-Pearson omnibus normality test was employed, along with tests for homoscedasticity. One-way ANOVA with multiple comparison tests (Tukey or Šidák) or two-tailed Student's *t*-test were used to determine statistical significance, with a *P*-value of less than 0.05 considered significant. Sample sizes are indicated in figure legends and graphs display individual data points as scatterplots. Data are presented with error bars representing the mean ± s.e.m. or mean ± s.d. Exclusion of samples or data occurred only in verified cases of technical error.

Acknowledgments

The authors would like to thank all members of the Boerckel lab for constructive discussions.

Funding

German Research Foundation grant LA 4007/2-1 (A.L.)

European Research Executive Agency (REA), Marie Skłodowska-Curie Global Postdoctoral Fellowship, Project 101063997 (HIPPOX) (A.L.)

National Institutes of Health grant R01 AR073809 (J.D.B.)

National Institutes of Health grant R01 AR074948 (J.D.B.)

National Institutes of Health grant P30 AR069619 (J.D.B.)

National Science Foundation Center for Engineering Mechanobiology CMMI 1548571 (J.D.B.)

National Institutes of Health grant U24 EB028941 (S.A.V.)

Author contributions

A.L. and J.D.B. conceived and supervised the research. A.L., J.D.B., M.N., M.P., Y.M. designed and performed animal experiments. A.L. and J.M.C. performed analysis. A.L. and C.K. performed EF5 experiments and analysis. A.L., S.B. and S.A.V. performed direct oxygen measurement and analysis. M.P., E.S., Y.Y., Y.F., M.G. supported with methods, technical guidance and advice. A.L. and J.D.B. wrote the paper. All authors discussed and revised the manuscript.

Competing interests

Authors declare that they have no competing interests. J.D.B. and A.L are named inventors on provisional US Patent application 63/626,981, filed by The Trustees of the University of Pennsylvania. This invention relates to devices and methods to modulate erythropoiesis and oxygen levels at the fracture site.

Data and materials availability

All data are available in the main text or the supplementary materials. The data discussed in this publication have been deposited in NCBI's Gene Expression Omnibus and are accessible through GEO Series accession number GSE230260 by request.

References

1 Swartz, H. M. *et al.* How best to interpret measures of levels of oxygen in tissues to make them effective clinical tools for care of patients with cancer and other oxygen-dependent pathologies. *Physiol Rep* **8**, e14541, doi:10.14814/phy2.14541 (2020).

2 Spencer, J. A. *et al.* Direct measurement of local oxygen concentration in the bone marrow of live animals. *Nature* **508**, 269-273, doi:10.1038/nature13034 (2014).

3 Carlier, A., Geris, L., van Gastel, N., Carmeliet, G. & Van Oosterwyck, H. Oxygen as a critical determinant of bone fracture healing-a multiscale model. *J Theor Biol* **365**, 247-264, doi:10.1016/j.jtbi.2014.10.012 (2015).

4 Claes, L., Recknagel, S. & Ignatius, A. Fracture healing under healthy and inflammatory conditions. *Nat Rev Rheumatol* **8**, 133-143, doi:10.1038/nrrheum.2012.1 (2012).

5 Yellowley, C. E. & Genetos, D. C. Hypoxia Signaling in the Skeleton: Implications for Bone Health. *Curr Osteoporos Rep* **17**, 26-35, doi:10.1007/s11914-019-00500-6 (2019).

6 Grundnes, O. & Reikerås, O. Blood flow and mechanical properties of healing bone. Femoral osteotomies studied in rats. *Acta Orthop Scand* **63**, 487-491, doi:10.3109/17453679209154720 (1992).

7 Schipani, E. *et al.* Hypoxia in cartilage: HIF-1alpha is essential for chondrocyte growth arrest and survival. *Genes Dev* **15**, 2865-2876, doi:10.1101/gad.934301 (2001).
8 Amarilio, R. *et al.* HIF1α regulation of Sox9 is necessary to maintain differentiation of hypoxic prechondrogenic cells during early skeletogenesis. *Development* **134**, 3917-3928, doi:10.1242/dev.008441 (2007).
9 Kolar, P., Gaber, T., Perka, C., Duda, G. N. & Buttgereit, F. Human early fracture hematoma is characterized by inflammation and hypoxia. *Clin Orthop Relat Res* **469**, 3118-3126, doi:10.1007/s11999-011-1865-3 (2011).
10 Komatsu, D. E. & Hadjiargyrou, M. Activation of the transcription factor HIF-1 and its target genes, VEGF, HO-1, iNOS, during fracture repair. *Bone* **34**, 680-688, doi:10.1016/j.bone.2003.12.024 (2004).
11 Stegen, S. *et al.* Adequate hypoxia inducible factor 1α signaling is indispensable for bone regeneration. *Bone* **87**, 176-186, doi:10.1016/j.bone.2016.03.014 (2016).
12 Wan, C. *et al.* Activation of the hypoxia-inducible factor-1alpha pathway accelerates bone regeneration. *Proc Natl Acad Sci U S A* **105**, 686-691, doi:10.1073/pnas.0708474105 (2008).
13 Lennon, D. P., Edmison, J. M. & Caplan, A. I. Cultivation of rat marrow-derived mesenchymal stem cells in reduced oxygen tension: effects on in vitro and in vivo osteochondrogenesis. *J Cell Physiol* **187**, 345-355, doi:10.1002/jcp.1081 (2001).
14 Pattappa, G., Johnstone, B., Zellner, J., Docheva, D. & Angele, P. The Importance of Physioxia in Mesenchymal Stem Cell Chondrogenesis and the Mechanisms Controlling Its Response. *Int J Mol Sci* **20**, doi:10.3390/ijms20030484 (2019).
15 Aro, H., Eerola, E., Aho, A. J. & Niinikoski, J. Tissue oxygen tension in externally stabilized tibial fractures in rabbits during normal healing and infection. *Journal of Surgical Research* **37**, 202-207, doi:10.1016/0022-4804(84)90181-1 (1984).
16 Brighton, C. T. & Krebs, A. G. Oxygen tension of healing fractures in the rabbit. *J Bone Joint Surg Am* **54**, 323-332 (1972).
17 Epari, D. R., Lienau, J., Schell, H., Witt, F. & Duda, G. N. Pressure, oxygen tension and temperature in the periosteal callus during bone healing--an in vivo study in sheep. *Bone* **43**, 734-739, doi:10.1016/j.bone.2008.06.007 (2008).
18 Lu, C. *et al.* Tibial fracture decreases oxygen levels at the site of injury. *Iowa Orthop J* **28**, 14-21 (2008).
19 Lu, C. *et al.* The role of oxygen during fracture healing. *Bone* **52**, 220-229, doi:10.1016/j.bone.2012.09.037 (2013).
20 Boerckel, J. D., Uhrig, B. A., Willett, N. J., Huebsch, N. & Guldberg, R. E. Mechanical regulation of vascular growth and tissue regeneration in vivo. *Proc Natl Acad Sci U S A* **108**, E674-680, doi:10.1073/pnas.1107019108 (2011).
21 Stefanowski, J. *et al.* Spatial Distribution of Macrophages During Callus Formation and Maturation Reveals Close Crosstalk Between Macrophages and Newly Forming Vessels. *Front Immunol* **10**, 2588, doi:10.3389/fimmu.2019.02588 (2019).
22 Koch, C. J. Measurement of absolute oxygen levels in cells and tissues using oxygen sensors and 2-nitroimidazole EF5. *Methods Enzymol* **352**, 3-31, doi:10.1016/s0076-6879(02)52003-6 (2002).
23 Koch, C. J. Importance of antibody concentration in the assessment of cellular hypoxia by flow cytometry: EF5 and pimonidazole. *Radiat Res* **169**, 677-688, doi:10.1667/rr1305.1 (2008).
24 Lord, E. M., Harwell, L. & Koch, C. J. Detection of hypoxic cells by monoclonal antibody recognizing 2-nitroimidazole adducts. *Cancer Res* **53**, 5721-5726 (1993).
25 Vanderkooi, J. M., Maniara, G., Green, T. J. & Wilson, D. F. An optical method for measurement of dioxygen concentration based upon quenching of phosphorescence. *J Biol Chem* **262**, 5476-5482 (1987).
26 Lebedev, A. Y. *et al.* Dendritic phosphorescent probes for oxygen imaging in biological systems. *ACS Appl Mater Interfaces* **1**, 1292-1304, doi:10.1021/am9001698 (2009).
27 Esipova, T. V. *et al.* Two new "protected" oxyphors for biological oximetry: properties and application in tumor imaging. *Anal Chem* **83**, 8756-8765, doi:10.1021/ac2022234 (2011).
28 Holland, S. K., Kennan, R. P., Schaub, M. M., D'Angelo, M. J. & Gore, J. C. Imaging oxygen tension in liver and spleen by 19F NMR. *Magnetic Resonance in Medicine* **29**, 446-458, doi:https://doi.org/10.1002/mrm.1910290405 (1993).
29 Stewart, I. B. & McKenzie, D. C. The Human Spleen During Physiological Stress. *Sports Medicine* **32**, 361-369, doi:10.2165/00007256-200232060-00002 (2002).
30 Boerckel, J. D. Created in BioRender: https://BioRender.com/r21q019. (2025).
31 Kovtun, A. *et al.* The crucial role of neutrophil granulocytes in bone fracture healing. *Eur Cell Mater* **32**, 152-162, doi:10.22203/ecm.v032a10 (2016).
32 Schlundt, C. *et al.* Macrophages in bone fracture healing: Their essential role in endochondral ossification. *Bone* **106**, 78-89, doi:10.1016/j.bone.2015.10.019 (2018).
33 Pevny, L. *et al.* Erythroid differentiation in chimaeric mice blocked by a targeted mutation in the gene for transcription factor GATA-1. *Nature* **349**, 257-260, doi:10.1038/349257a0 (1991).

34 Yamamoto, M. *et al.* Activity and tissue-specific expression of the transcription factor NF-E1 multigene family. *Genes Dev* **4**, 1650-1662, doi:10.1101/gad.4.10.1650 (1990).
35 Chen, K. *et al.* Resolving the distinct stages in erythroid differentiation based on dynamic changes in membrane protein expression during erythropoiesis. *Proceedings of the National Academy of Sciences* **106**, 17413-17418, doi:10.1073/pnas.0909296106 (2009).
36 Yien, Y. Y. & Perfetto, M. Regulation of Heme Synthesis by Mitochondrial Homeostasis Proteins. *Frontiers in Cell and Developmental Biology* **10** (2022).
37 Zhang, F. *et al.* An extra-erythrocyte role of haemoglobin body in chondrocyte hypoxia adaption. *Nature* **622**, 834-841, doi:10.1038/s41586-023-06611-6 (2023).
38 Burmester, T., Weich, B., Reinhardt, S. & Hankeln, T. A vertebrate globin expressed in the brain. *Nature* **407**, 520-523, doi:10.1038/35035093 (2000).
39 Gödecke, A. *et al.* Disruption of myoglobin in mice induces multiple compensatory mechanisms. *Proc Natl Acad Sci U S A* **96**, 10495-10500, doi:10.1073/pnas.96.18.10495 (1999).
40 Liu, L., Zeng, M. & Stamler, J. S. Hemoglobin induction in mouse macrophages. *Proceedings of the National Academy of Sciences* **96**, 6643-6647, doi:10.1073/pnas.96.12.6643 (1999).
41 Tusi, B. K. *et al.* Population snapshots predict early haematopoietic and erythroid hierarchies. *Nature* **555**, 54-60, doi:10.1038/nature25741 (2018).
42 Koulnis, M. *et al.* Identification and analysis of mouse erythroid progenitors using the CD71/TER119 flow-cytometric assay. *J Vis Exp*, doi:10.3791/2809 (2011).
43 Hentze, M. W., Muckenthaler, M. U. & Andrews, N. C. Balancing Acts: Molecular Control of Mammalian Iron Metabolism. *Cell* **117**, 285-297, doi:https://doi.org/10.1016/S0092-8674(04)00343-5 (2004).
44 Ponka, P. Tissue-Specific Regulation of Iron Metabolism and Heme Synthesis: Distinct Control Mechanisms in Erythroid Cells. *Blood* **89**, 1-25, doi:10.1182/blood.V89.1.1 (1997).
45 Matos, M. A., Araújo, F. P. & Paixão, F. B. Histomorphometric evaluation of bone healing in rabbit fibular osteotomy model without fixation. *Journal of Orthopaedic Surgery and Research* **3**, 4, doi:10.1186/1749-799X-3-4 (2008).
46 Donneys, A. *et al.* Localized deferoxamine injection augments vascularity and improves bony union in pathologic fracture healing after radiotherapy. *Bone* **52**, 318-325, doi:10.1016/j.bone.2012.10.014 (2013).
47 Lang, A. *et al.* MIF does only marginally enhance the pro-regenerative capacities of DFO in a mouse-osteotomy-model of compromised bone healing conditions. *Bone* **154**, 116247, doi:10.1016/j.bone.2021.116247 (2022).
48 Chow, A. *et al.* CD169^{+} macrophages provide a niche promoting erythropoiesis under homeostasis and stress. *Nat Med* **19**, 429-436, doi:10.1038/nm.3057 (2013).
49 Ramos, P. *et al.* Macrophages support pathological erythropoiesis in polycythemia vera and β-thalassemia. *Nat Med* **19**, 437-445, doi:10.1038/nm.3126 (2013).
50 Batoon, L. *et al.* CD169(+) macrophages are critical for osteoblast maintenance and promote intramembranous and endochondral ossification during bone repair. *Biomaterials* **196**, 51-66, doi:10.1016/j.biomaterials.2017.10.033 (2019).
51 McDermott, A. M. *et al.* Recapitulating bone development through engineered mesenchymal condensations and mechanical cues for tissue regeneration. *Sci Transl Med* **11**, doi:10.1126/scitranslmed.aav7756 (2019).
52 Gerber, H.-P. *et al.* VEGF couples hypertrophic cartilage remodeling, ossification and angiogenesis during endochondral bone formation. *Nature Medicine* **5**, 623-628, doi:10.1038/9467 (1999).
53 Maes, C. *et al.* Impaired angiogenesis and endochondral bone formation in mice lacking the vascular endothelial growth factor isoforms VEGF164 and VEGF188. *Mech Dev* **111**, 61-73, doi:10.1016/s0925-4773(01)00601-3 (2002).
54 Hankenson, K. D., Dishowitz, M., Gray, C. & Schenker, M. Angiogenesis in bone regeneration. *Injury* **42**, 556-561, doi:https://doi.org/10.1016/j.injury.2011.03.035 (2011).
55 Lang, A. *et al.* Cyr61 delivery promotes angiogenesis during bone fracture repair. *bioRxiv*, 2024.2004.2005.588239, doi:10.1101/2024.04.05.588239 (2024).
56 van Gastel, N. *et al.* Lipid availability determines fate of skeletal progenitor cells via SOX9. *Nature* **579**, 111-117, doi:10.1038/s41586-020-2050-1 (2020).
57 Lambeth, J. D. NOX enzymes and the biology of reactive oxygen. *Nature Reviews Immunology* **4**, 181-189, doi:10.1038/nri1312 (2004).
58 Pedroza-Dávila, U. *et al.* Metabolism, ATP production and biofilm generation by Staphylococcus epidermidis in either respiratory or fermentative conditions. *AMB Express* **10**, 31, doi:10.1186/s13568-020-00966-z (2020).
59 Anup, A. *et al.* Embracing ethical research: Implementing the 3R principles into fracture healing research for sustainable scientific progress. *J Orthop Res* **42**, 568-577, doi:10.1002/jor.25741 (2024).
60 Röntgen, V. *et al.* Fracture healing in mice under controlled rigid and flexible conditions using an adjustable external fixator. *J Orthop Res* **28**, 1456-1462, doi:10.1002/jor.21148 (2010).
61 Jirkof, P. *et al.* Administration of Tramadol or Buprenorphine via the drinking water for post-operative analgesia in a mouse-osteotomy model. *Sci Rep* **9**, 10749, doi:10.1038/s41598-019-47186-5 (2019).

62 Wolter, A. *et al.* A buprenorphine depot formulation provides effective sustained post-surgical analgesia for 72 h in mouse femoral fracture models. *Sci Rep* **13**, 3824, doi:10.1038/s41598-023-30641-9 (2023).
63 Chong, S. H. *et al.* Real-time tracking of brain oxygen gradients and blood flow during functional activation. *Neurophotonics* **9**, 045006, doi:10.1117/1.NPh.9.4.045006 (2022).
64 Friedman, E. S. *et al.* Microbes vs. chemistry in the origin of the anaerobic gut lumen. *Proc Natl Acad Sci U S A* **115**, 4170-4175, doi:10.1073/pnas.1718635115 (2018).
65 El Khatib, M. *et al.* Ultrafast Tracking of Oxygen Dynamics During Proton FLASH. *Int J Radiat Oncol Biol Phys* **113**, 624-634, doi:10.1016/j.ijrobp.2022.03.016 (2022).
66 Hao, Y. *et al.* Integrated analysis of multimodal single-cell data. *Cell* **184**, 3573-3587.e3529, doi:10.1016/j.cell.2021.04.048 (2021).

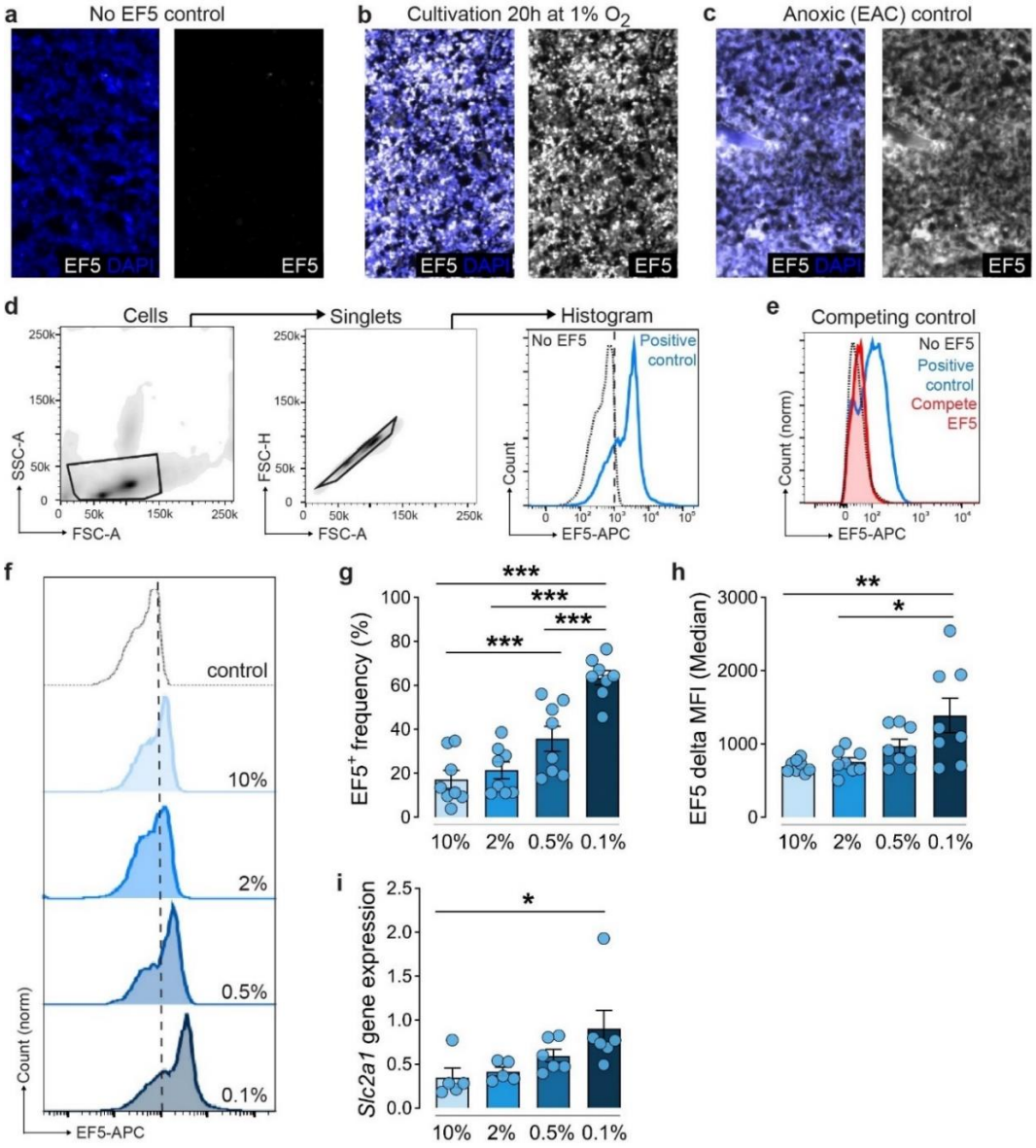

Extended Data Figure 1: EF5 staining marks hypoxic cells. To identify hypoxic cells, we injected mice with EF5, which, in the absence of intracellular oxygen, is reduced by nitroreductase enzymes to form cytoplasmic EF5-protein adducts that can be identified by immunostaining. To setup the staining process for cryosections, different controls were used: (**a**) no EF5 control, (**b**) murine femora were cultivated ex vivo for 20h at 1% (fraction of oxygen) with adding EF5 compound during the last 2h and (**c**) mice were injected with EF5 compound and euthanized after 30 min. The body was then kept at 37°C for 45 min allowing tissue metabolism to create severe hypoxia and reduce all EF5 in situ (euthanized animal control, EAC). Representative images from n = 3-4 mice per group in 3 independent experiments. (**d**) Gating strategy for analysis of $EF5^+$ cell frequency. (**e**) Competed-stain control. EF5 compound (which competitively inhibits Ab staining to EF5 cellular adducts) was added to the staining antibody mixture and shortly pre-incubated before being added to the isolated cells. Representative histogram for n = 2 in 2 independent experiments. (**f**) Cells isolated from the bone marrow were cultivated for 1h at different levels of pO_2 (represented by fractions of oxygen) to confirm staining specificity as indicated by the (**g**) $EF5^+$ cell frequency, (**h**) EF5 delta median fluorescence intensity and (**i**) expression of hypoxia-relevant gene. Data show individual data points for n = 4 mice from 2 independent experiments and are mean ± s.e.m. *P* values were calculated using one-way ANOVA with Šidák multiple comparison test for preselected pairs. $*P < 0.05$, $**P < 0.01$ and $***P < 0.001$.

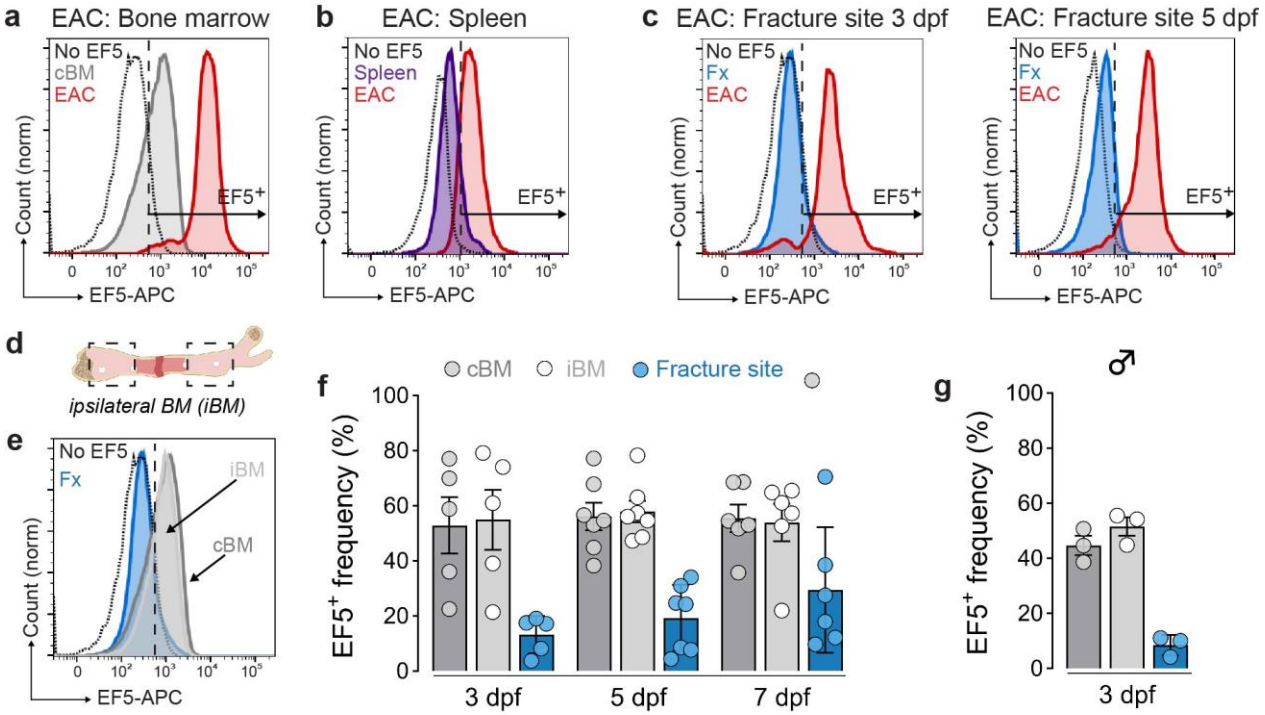

Extended Data Figure 2: EF5 staining marks hypoxic cells at the fracture site. To verify EF5 distribution and capacity to mark hypoxic cells at the fracture site, we performed a control experiment to induce anoxia. Mice were injected with EF5 compound and euthanized after 30 min. The body was then kept at 37°C in anoxic conditions for 45 min (euthanized animal control, EAC). (**a-c**) EAC controls in bone marrow, spleen and the fracture site 3 and 5 dpf demonstrate EF5 distribution in the tissue and EF5 dynamic range in vivo. Representative histograms from n = 2 mice in 2 independent experiments. (**d**) We refer to the ipsilateral bone marrow (iBM) as the bone marrow regions in the injured bone but distant from the fracture site. (**e**) Flow cytometry analysis of EF5 staining displaying representative histogram of non-EF5 staining control, iBM, cBM, and fracture site and (**f**) quantification of $EF5^+$ cell frequencies at 3, 5 and 7 dpf. These experiments were performed in female mice. Data show individual data points for n = 5 mice from at least 3 independent experiments and are mean ± s.e.m. (**g**) Male mice exhibit equivalent response. Data show individual data points for n = 3 mice and are mean ± s.e.m.

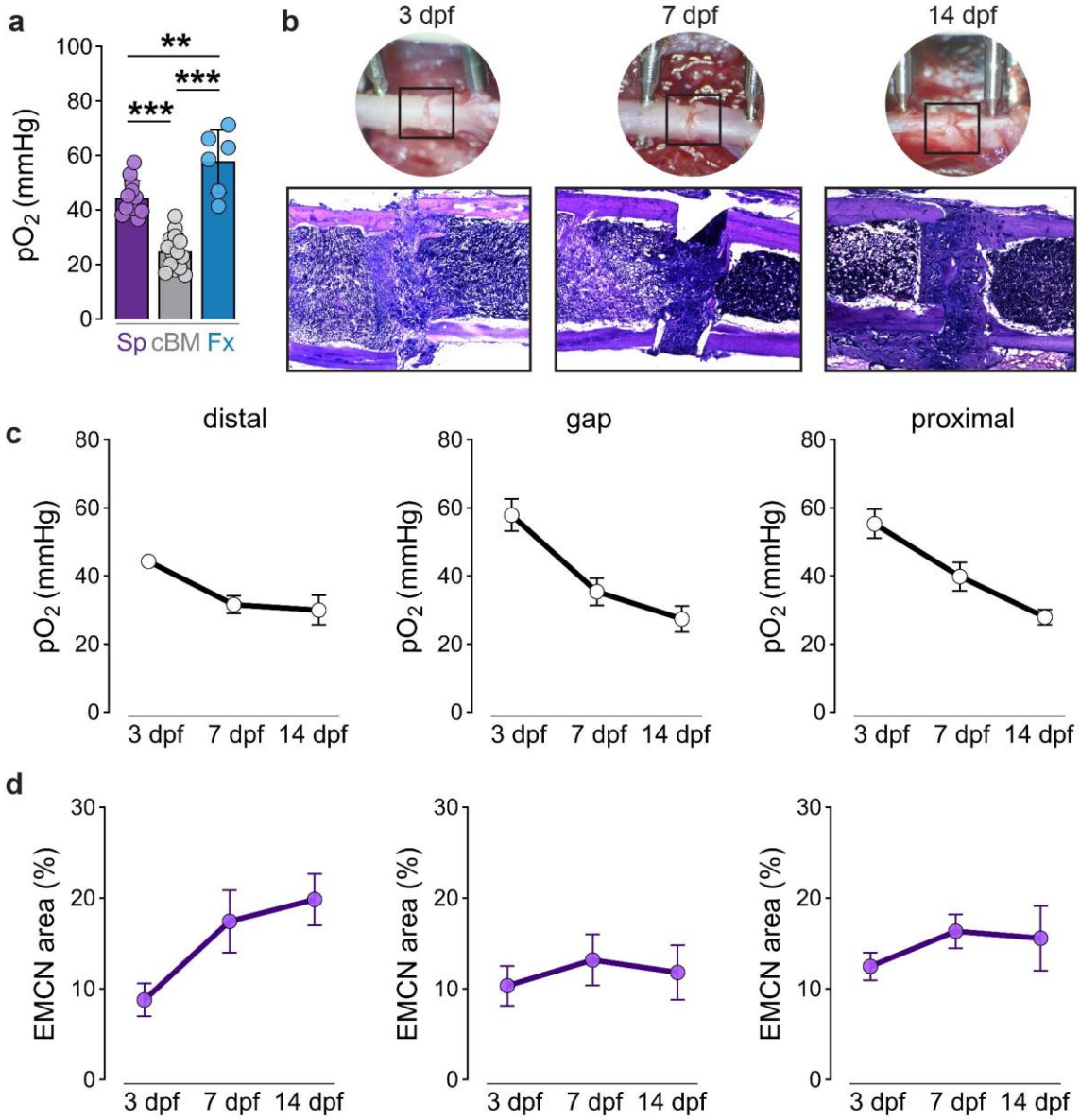

Extended Data Figure 3: Direct oxygen measurement at the fracture site. (**a**) Direct oxygen measurement in the spleen (Sp) compared to cBM and fracture site at 3 dpf (Fx). Data show individual data points for n = 6-14 mice at least 3 independent experiments and are mean ± s.d. *P* values were calculated using one-way ANOVA with Tukey multiple comparison test. ***P* < 0.01 and ****P* < 0.001. (**b**) Macroscopic views on the fracture site at 3, 7 and 14 dpf and HE staining to display cellular changes at the fracture site. Representative images from for n = 4-6 mice per group and timepoint from at least 2 independent experiments. (**c**-**d**) Separate displays of temporal development of (**c**) pO_2 values and (**d**) $EMCN^+$ areas in the distal, gap and proximal fracture site. Data are mean ± s.e.m. for n = 4-6 mice per group and timepoint from at least 2 independent experiments.

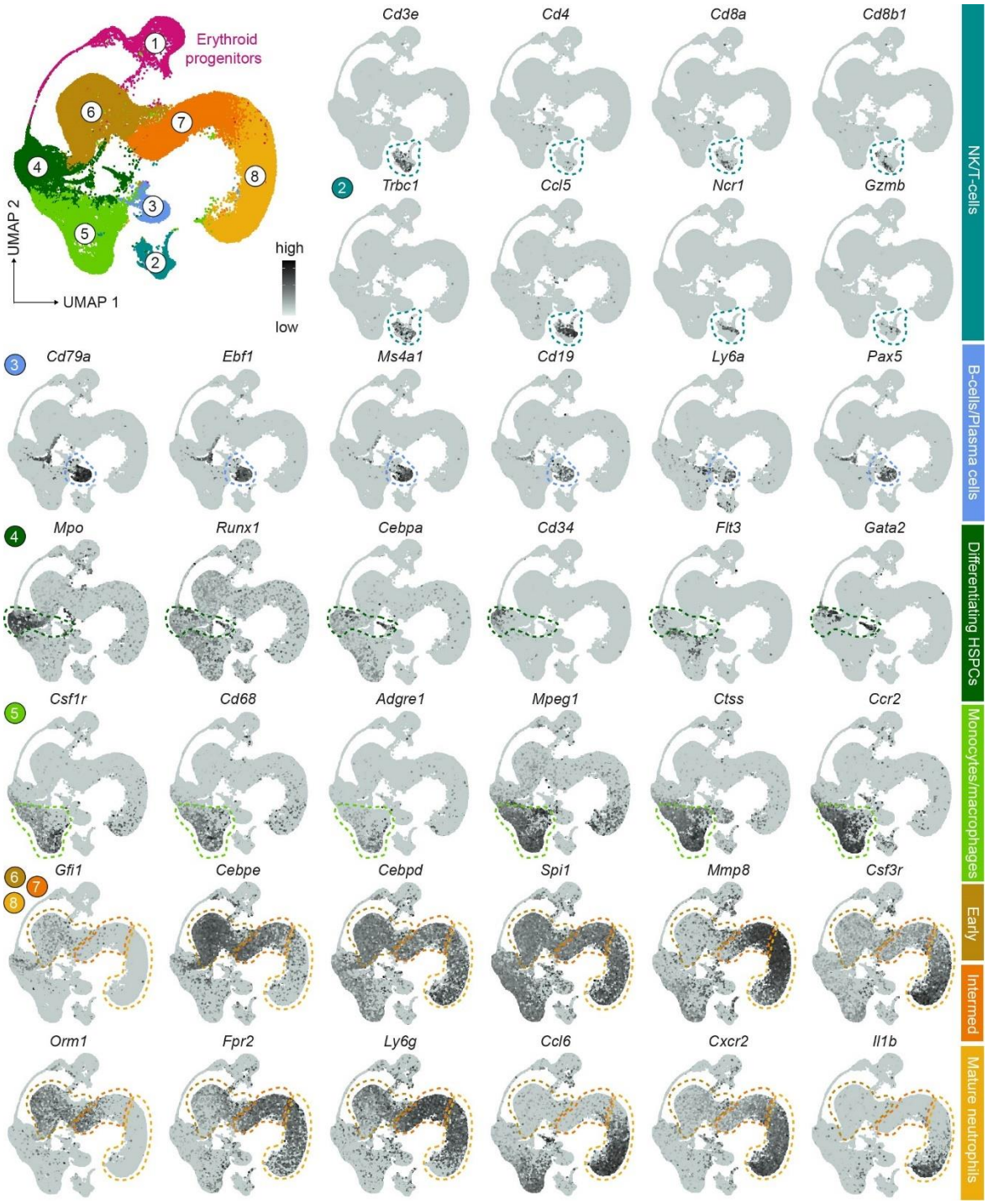

Extended Data Figure 4: Canonical marker gene expression to identify major cell populations at the fracture site at 3 dpf. Louvain clustering resulted in 8 clusters, which were assigned to the respective cell populations. Feature plots indicate relevant genes on the UMAP.

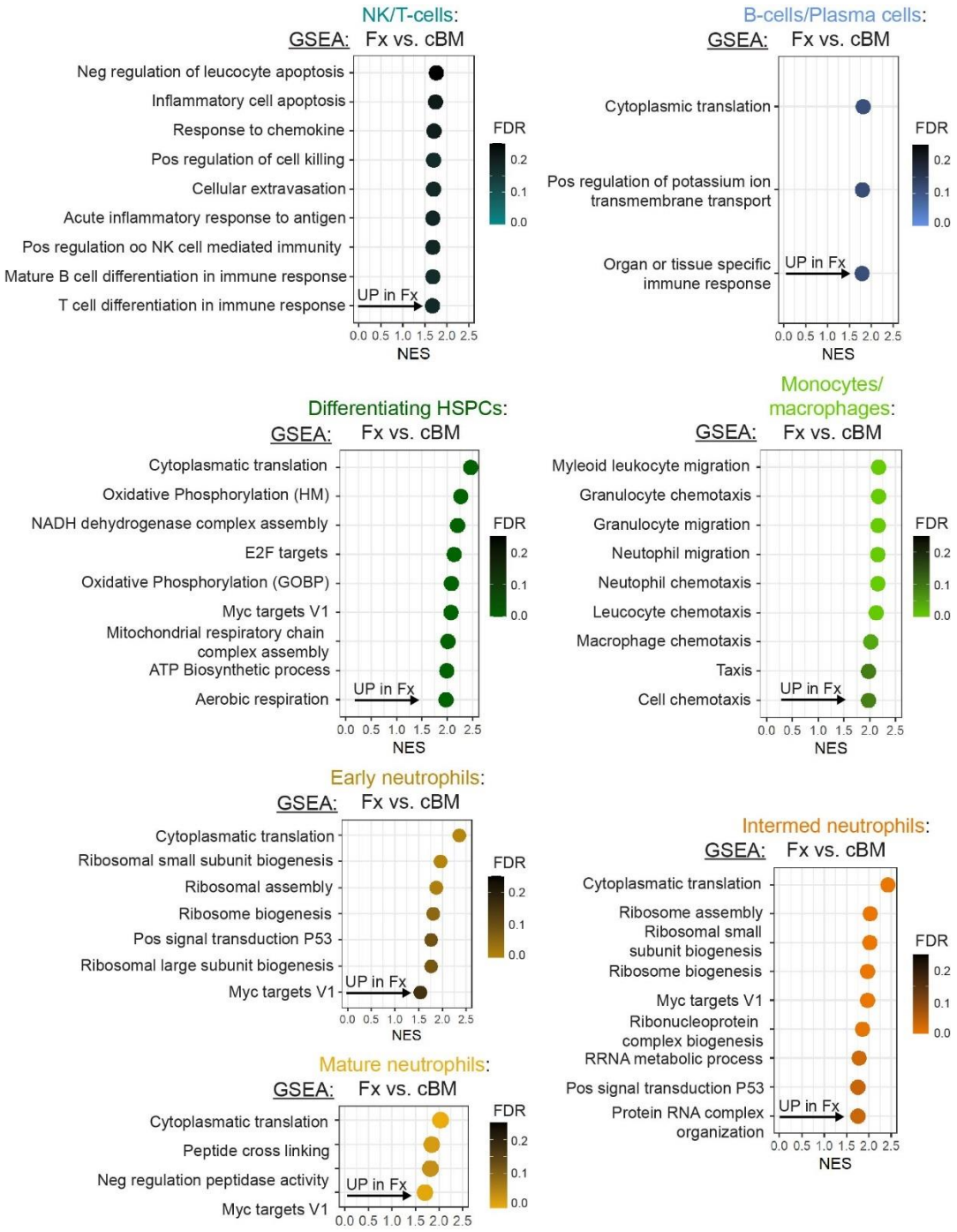

Extended Data Figure 5: Gene set enrichment analysis (GSEA) for major cell populations at the fracture site at 3 dpf. A pre-ranked list of genes was generated based on fold changes between comparisons. The murine hallmark gene set collection and the GO Biological Process ontology from the Molecular Signatures Database (MSigDB) was used for analysis. We identified activation of HSPCs and adaptive immune cells (T- and B-cells) at the fracture site. Further, innate immune cells, including monocytes, macrophages and granulocytes showed pathway enrichment of known inflammation kinetics.

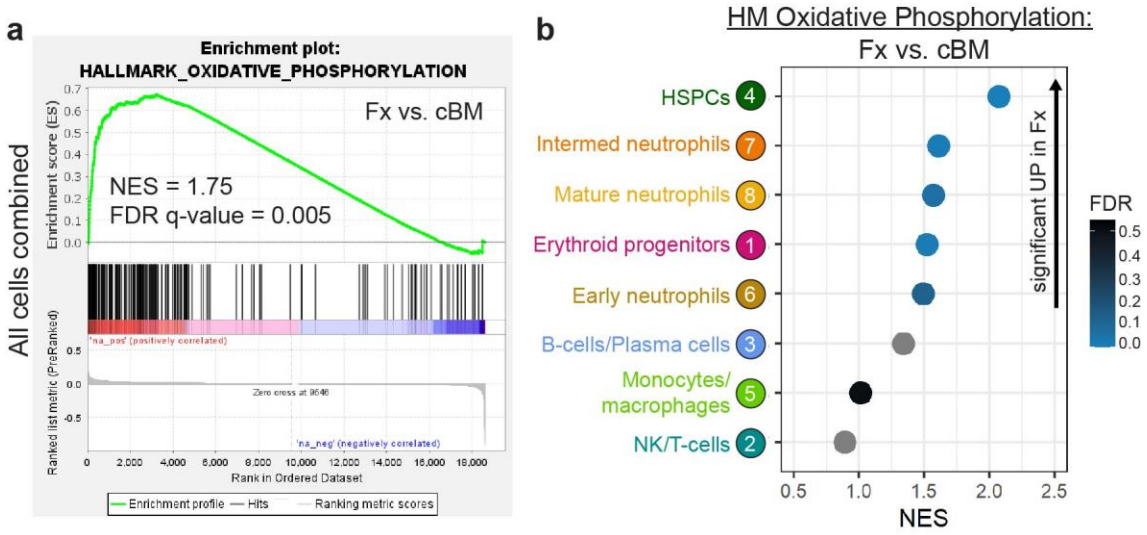

Extended Data Figure 6: Analysis of genes relevant in oxidative phosphorylation. (**a**) GSEA on all cells combined (3 dpf): enrichment plot shows comparison with hallmark gene set oxidative phosphorylation indicating significant higher expression at the fracture site when compared to the contralateral bone marrow. (**b**) GSEA separated for cell populations indicates that genes involved in oxidative phosphorylation are, particularly higher expressed in HSPCs, neutrophils, and erythroid progenitors.

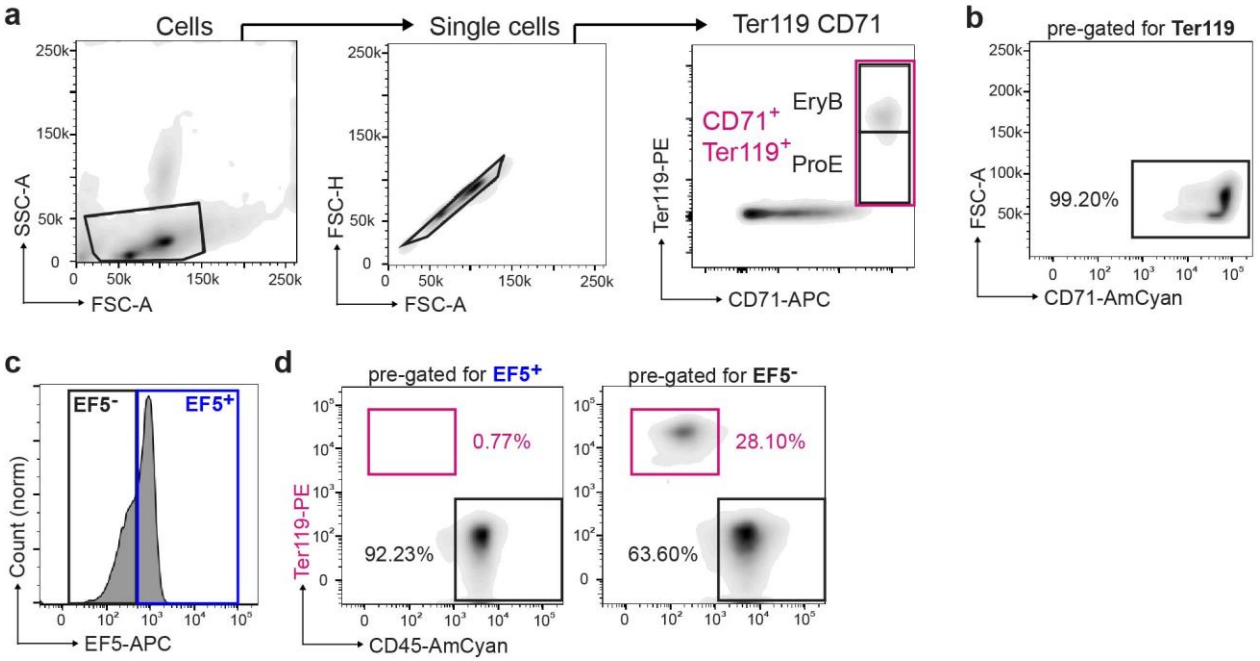

Extended Data Figure 7: Gating and analysis strategy for CD71⁺ Ter119⁺ erythroid cells in the bone marrow. (**a**) Gating strategy for analysis of CD71⁺ Ter119⁺ cell frequency. (**b**) Detailed gating on Ter119⁺ cells confirming positive dual staining for CD71. (**c**) Uninjured bone marrow contains both EF5⁺ and EF5⁻ cells. Representative histogram of EF5 staining in bone marrow to indicate gating for EF5⁻ and EF5⁺ cells. (**d**) Of EF5⁺ cells, only 0.77 ± 0.5% were Ter119⁺ CD45⁻ erythroid cells, while of the EF5⁻ cells, 28.1 ± 8.5% of EF5⁻ cells were of erythroid lineage (mean ± s.d. for n = 4 mice from 4 independent experiments).

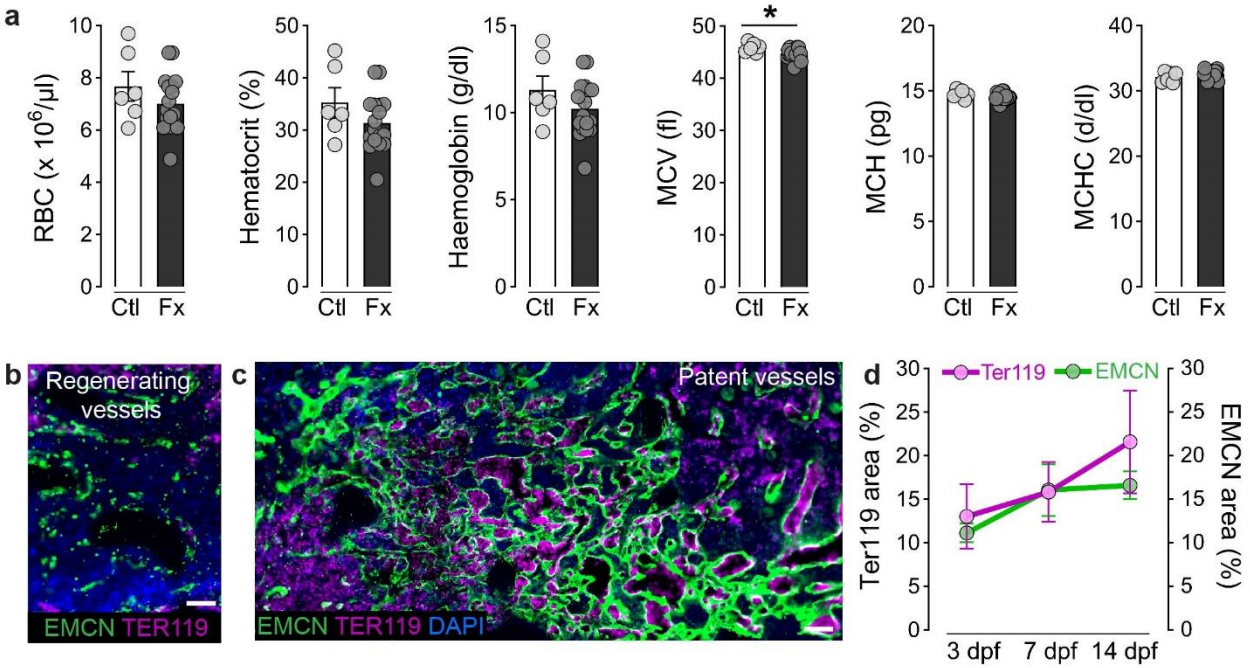

Extended Data Figure 8: Bone fracture activates local erythropoiesis at the fracture site. (**a**) Blood parameters measured in peripheral blood at 3 dpf. Data show individual data points from n = 6-17 mice from more than 5 independent experiments and are mean ± s.e.m. *P* values were calculated using two-tailed Student's *t*-test. **P* < 0.05. (**b, c**) Representative images of Ter119 staining at the fracture site at 3 dpf. (**b**) After injury, regenerating vessels do not contain Ter119$^+$ erythrocytes compared to (**c**) patent vessels. Scale bars, 50 µm. Representative images for n = 4-8 mice per timepoint from 3 independent experiments. (**d**) Quantification of Ter119$^+$ area and EMCN$^+$ area at the fracture site over time shows that the presence of erythrocytes depends on vascular regeneration. Data are mean ± s.e.m. for n = 4-8 mice per timepoint from 3 independent experiments. *P* values were calculated using one-way ANOVA with Tukey multiple comparison test.

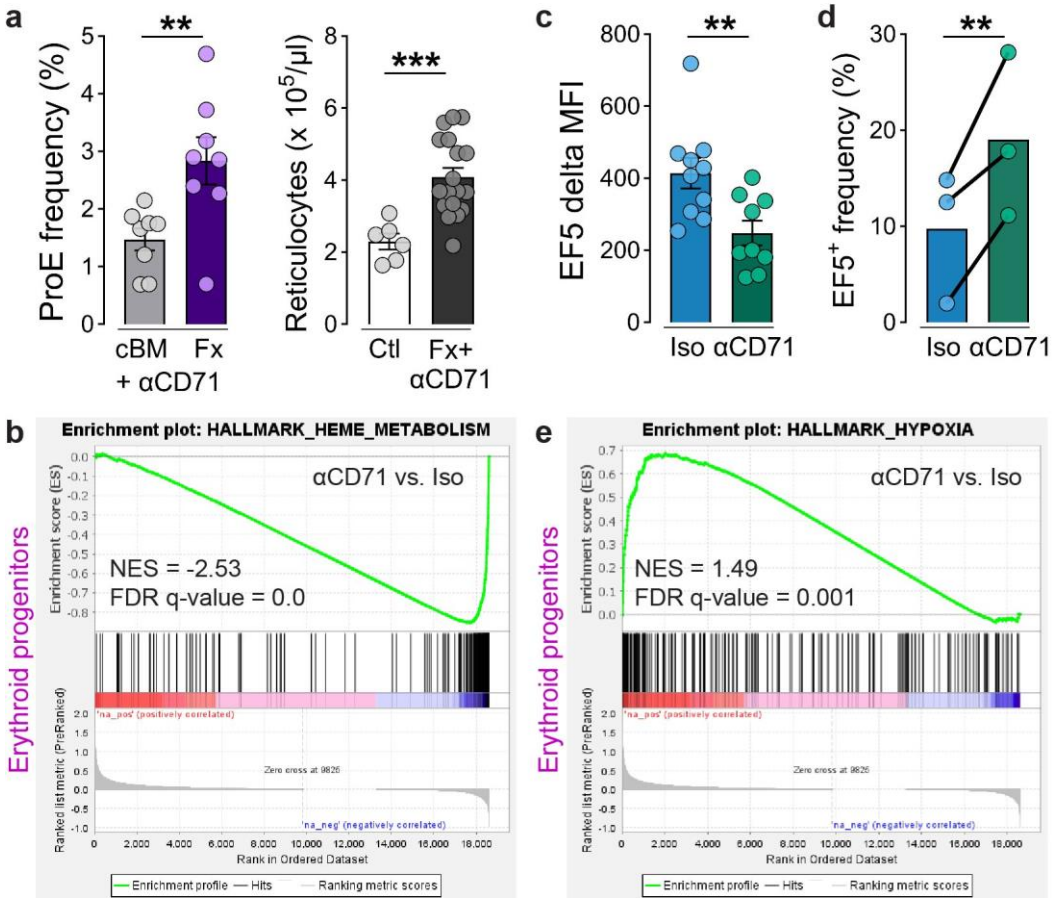

Extended Data Figure 9: CD71 blockade does not affect erythropoiesis *per se* but induces hypoxia. (**a**) Frequency of ProE (Ter119^{med} CD71^{high}) at fracture site and concentration of reticulocytes in peripheral blood 3 dpf. Data show individual data points from n = 6-18 mice from more than 3 independent experiments and are mean ± s.e.m. *P* values were calculated using two-tailed Student's *t*-test. (**b**) GSEA on erythroid progenitor cluster: enrichment plot shows comparison with hallmark gene set haem metabolism indicating significant lower expression with CD71 antibody treatment. (**c**) Quantification delta EF5 MFI to cBM including all cells. Data show individual data points for n = 8-9 mice per group from 5 independent experiments and are mean ± s.e.m. *P* values were calculated using two-tailed Student's *t*-test. MFI, median fluorescence intensity. (**d**) Flow cytometry analysis of erythroid lineage cells (CD71$^+$ Ter119$^+$) and their EF5 staining intensity - representation of paired samples per experiment. Data show individual data points for n = 3-5 mice per group from 3 independent experiments and are mean ± s.e.m. *P* values were calculated using two-tailed paired Student's *t*-test. (**e**) GSEA on erythroid progenitor cluster: enrichment plot shows comparison with hallmark gene set hypoxia indicating significant higher expression with CD71 antibody treatment. $^{**}P < 0.01$ and $^{***}P < 0.001$.

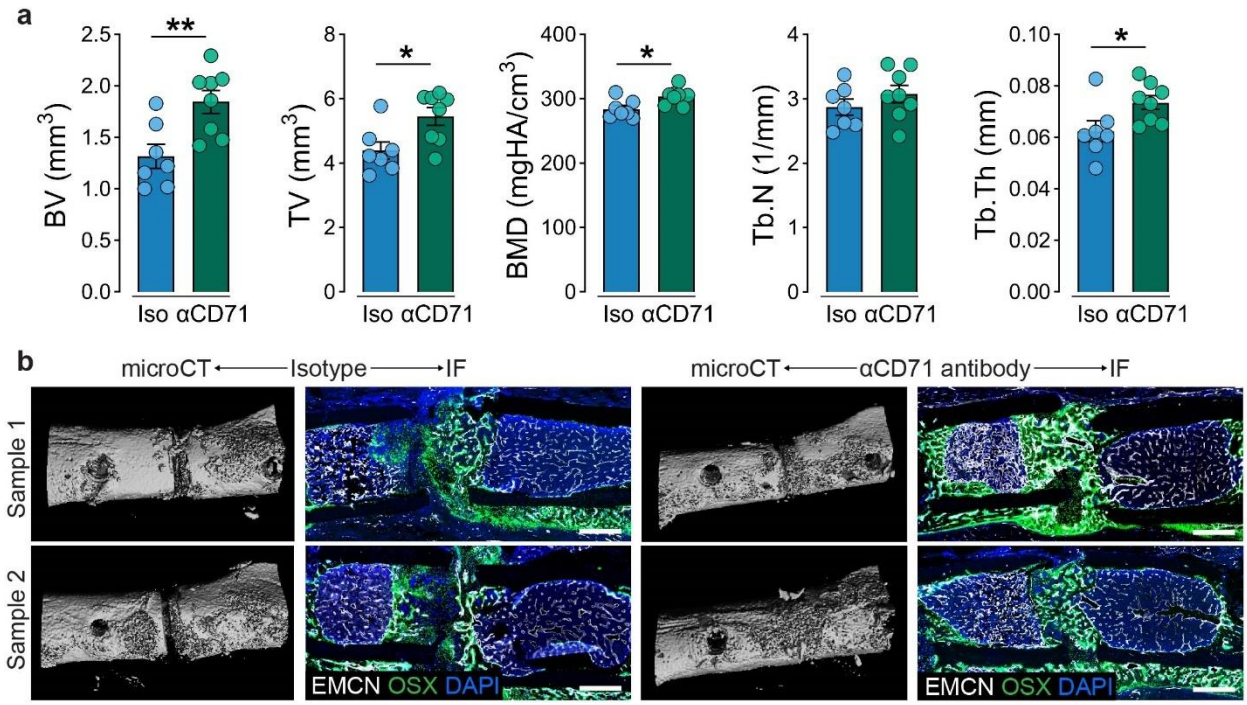

Extended Data Figure 10: CD71 blockade promotes bone regeneration at 14 dpf. (**a**) MicroCT analysis of bone morphometry. Data show individual data points for n = 9-10 mice per group from 2 independent experiments and are mean ± s.e.m. *P* values were calculated using two-tailed Student's *t*-test. $*P < 0.05$, $**P < 0.01$ and $***P < 0.001$. (**b**) Additional samples: macroscopic 3D microCT reconstruction and corresponding immunofluorescence images of $EMCN^+$ vessel formation and OSX^+ progenitor infiltration at the fracture site at 14 dpf. Scale bars, 500 µm.